This is a repository copy of *Nonlinear evolution of vortical disturbances entrained in the entrance region of a circular pipe*.

White Rose Research Online URL for this paper:
https://eprints.whiterose.ac.uk/220650/

Version: Accepted Version

Article:

Zhu, K. orcid.org/0000-0002-9450-9662 and Ricco, P. orcid.org/0000-0003-1537-1667 (2024) Nonlinear evolution of vortical disturbances entrained in the entrance region of a circular pipe. Journal of Fluid Mechanics, 998. A19. ISSN 0022-1120

https://doi.org/10.1017/jfm.2024.882

© 2024 The Authors. Except as otherwise noted, this author-accepted version of a journal article published in Journal of Fluid Mechanics is made available via the University of Sheffield Research Publications and Copyright Policy under the terms of the Creative Commons Attribution 4.0 International License (CC-BY 4.0), which permits unrestricted use, distribution and reproduction in any medium, provided the original work is properly cited. To view a copy of this licence, visit http://creativecommons.org/licenses/by/4.0/

Reuse

This article is distributed under the terms of the Creative Commons Attribution (CC BY) licence. This licence allows you to distribute, remix, tweak, and build upon the work, even commercially, as long as you credit the authors for the original work. More information and the full terms of the licence here: https://creativecommons.org/licenses/

Takedown

If you consider content in White Rose Research Online to be in breach of UK law, please notify us by emailing eprints@whiterose.ac.uk including the URL of the record and the reason for the withdrawal request.

eprints@whiterose.ac.uk
https://eprints.whiterose.ac.uk/

Banner appropriate to article type will appear here in typeset article

Nonlinear evolution of vortical disturbances entrained in the entrance region of a circular pipe

Kaixin Zhu[1] **and Pierre Ricco**[1] †

[1] School of Mechanical, Aerospace and Civil Engineering, The University of Sheffield, Sheffield, S1 3JD, UK

(Received xx; revised xx; accepted xx)

Accepted in J. Fluid Mech. (2024).

The nonlinear evolution of free-stream vortical disturbances entrained in the entrance region of a circular pipe is investigated using asymptotic and numerical methods. Attention is focused on the low-frequency disturbances that induce streamwise elongated structures. A pair of vortical modes with opposite azimuthal wavenumbers is used to model the free-stream disturbances. Their amplitude is assumed to be intense enough for nonlinear interactions to occur inside the pipe. The formation and evolution of the perturbation flow are described by the nonlinear unsteady boundary-region equations in the cylindrical coordinate system, derived and solved herein for the first time. Matched asymptotic expansions are employed to construct appropriate initial conditions and the initial-boundary value problem is solved numerically by a marching procedure in the streamwise direction. Numerical results show the stabilising effect of nonlinearity on the intense algebraic growth of the disturbances and an increase of the wall-shear stress due to the nonlinear interactions. A parametric study is carried out to evince the effect of the Reynolds number, the streamwise and azimuthal wavelengths, and the radial length scale of the inlet disturbance on the nonlinear flow evolution. Elongated pipe-entrance nonlinear structures (EPENS) occupying the whole pipe cross-section are discovered. EPENS with h-fold rotational symmetry comprise h high-speed streaks positioned near the wall, and h low-speed streaks centred around the pipe core. These distinct structures display a striking resemblance to nonlinear travelling waves found numerically and observed experimentally in fully developed pipe flow. Good agreement of our mean-flow and root mean square data with experimental measurements is obtained.

Key words:

1. Introduction

As one of the most long-standing problems in fluid dynamics, stability and transition in pipe flow have puzzled engineers and scientists since the prominent experimental work of Reynolds (1883). Due to wide industrial applications, engineers have aimed to design efficient and durable pipeline systems by estimating the conditions under which the pipe flow

---

† Email address for correspondence: p.ricco@sheffield.ac.uk

is laminar or turbulent. This objective is driven by the large difference in pressure gradient required to drive laminar and turbulent flows in a pipe. Scientists have also been intrigued by the enigmatic physical mechanisms behind the instability and transition phenomena observed in experiments.

Earlier investigations of pipe flow date back to the independent studies of Hagen (1839) and Poiseuille (1844), where the linear relationship between pressure drop and volume flow rate for laminar flow was obtained. This relationship is now known as the Hagen-Poiseuille law, which holds only sufficiently downstream where the flow is fully developed, i.e. the velocity distribution is independent of the streamwise coordinate and its profile is parabolic. Near the pipe inlet, the velocity field varies in the streamwise direction and the terminologies developing pipe flow and pipe entrance flow are adopted. Considerable research effort has been focused on the stability and transition of the fully developed region, but much less attention has been devoted to the flow in the entrance region of the pipe. In this paper, we thus aim to investigate how free-stream vortical disturbances are entrained in the entrance region of a circular pipe and how the induced disturbances grow and evolve nonlinearly inside the pipe.

1.1. *Fully developed pipe flow*

The stability and transition of fully developed laminar pipe flow cannot be explained by the classical linear stability theory because the parabolic profile is stable to infinitesimally small disturbances. The reader is referred to Rayleigh (1892), Sexl (1927), Pekeris (1948), Corcos & Sellars (1959) and Gill (1965) for theoretical studies, and to Davey & Drazin (1969), Crowder & Dalton (1971), Garg & Rouleau (1972), Salwen & Grosch (1972) and Meseguer & Trefethen (2003) for numerical studies. However, transition in pipe flow is usually observed in experiments at moderate Reynolds numbers. This discrepancy has led to the inclusion of nonlinear effects in the study of pipe-flow stability. Weakly nonlinear theory was first applied independently by Davey & Nguyen (1971) and Itoh (1977), but the results contradicted each other. Davey & Nguyen (1971) reported that fully developed pipe flow was unstable to small but finite axisymmetric centre-mode disturbances when the disturbance amplitude exceeded a critical value, while the flow was found to be stable by Itoh (1977). The problem was reexamined by Davey (1978), who suggested that neither of those results was reliable. Direct numerical simulations performed by Patera & Orszag (1981) failed to find any finite-amplitude axisymmetric equilibria and suggested that the use of weakly nonlinear theory away from the neutral stability curve may be invalid. Smith & Bodonyi (1982) identified neutral disturbances of finite amplitude by employing the nonlinear critical layer theory.

The research interest then shifted from solving the eigenvalue problem established by the modal stability theory to the temporal initial value problem pertaining to the non-modal stability theory. Since the linear stability theory captures the long-time disturbance behaviour but overlooks the short-time behaviour (Kerswell 2005; Schmid 2007), at short times, disturbances may experience algebraic transient growth before the ultimate exponential decay (e.g., Böberg & Brösa 1988). One related approach is to identify the optimal disturbance that achieves the maximum transient energy growth. Studies on transient growth in time have revealed that optimal disturbances have a vanishing streamwise wavenumber and a unity azimuthal wavenumber (Bergström 1992; Schmid & Henningson 1994; O'Sullivan & Breuer 1994). Bergström (1993) and Schmid & Henningson (1994) also extended the work to disturbances with small but non-zero streamwise wavenumber. The spatial transient growth has been reported by Tumin (1996) and Reshotko & Tumin (2001). Stationary disturbances were found to exhibit a more significant amplification than non-stationary ones (Reshotko & Tumin 2001). Optimal disturbances provide the upper bound for the possible energy amplification, which is optimised over all possible initial conditions.

Faisst & Eckhardt (2003) and Wedin & Kerswell (2004) independently discovered nonlinear travelling waves in pipe flow for the first time, which were later observed in the experiments of Hof *et al.* (2004) and Hof *et al.* (2005). Inspired by these results, the nonlinear dynamical system approach has become a valuable tool in the last two decades (Eckhardt *et al.* 2007; Avila *et al.* 2023). From the perspective of dynamical theory, all initial conditions of the pipe-flow system that ultimately converge to the laminar state form the basin of attraction of the laminar state. Transition occurs when the initial conditions are outside of this basin boundary. The nonlinear non-modal stability theory describes the dynamics of finite disturbances within and beyond the basin boundary (Kerswell *et al.* 2014; Kerswell 2018). Optimisation methods have been utilised within this nonlinear theory to compute the so-called minimal seed (Pringle & Kerswell 2010; Pringle *et al.* 2012), i.e. the disturbance with the smallest energy for turbulence to occur. The interested reader is referred to Kerswell (2018) for an exhaustive review.

1.2. *Pipe-entrance flow*

The absence of linear instability in fully developed pipe flow directed interest to the flow in the developing entrance region. As the uniform flow enters the pipe inlet, a laminar boundary layer grows along the wall. One can then expect this pipe-entrance boundary layer to be linearly unstable. Research efforts first focused on the computation of the velocity and pressure distributions of this base flow (Langhaar 1942; Hornbeck 1964; Sparrow *et al.* 1964; Christiansen & Lemmon 1965).

The first temporal stability analysis of the pipe entrance flow was performed by Tatsumi (1952) by using a boundary-layer model that revealed the linear instability of the flow subjected to axisymmetric disturbances. The same problem was investigated numerically by Huang & Chen (1974*a*) and generalised to non-axisymmetric disturbances (Huang & Chen 1974*b*; Shen *et al.* 1976) and spatially unstable disturbances (Gupta & Garg 1981; Garg 1981; Garg & Gupta 1981; Garg 1983). Considerable discrepancies were observed among the results obtained in these studies, which may be attributed to the varying accuracies in the calculation of the laminar base flow (da Silva & Moss 1994). da Silva & Moss (1994) reexamined this stability problem with improved accuracy, obtaining good agreement with results by Gupta & Garg (1981). The critical Reynolds number based on the pipe radius was approximately 10 000 in both studies.

Although these studies focused on the stability of flow profiles at different streamwise locations in the pipe entrance, the receptivity problem - i.e. how entrained free-stream disturbances excite instability in the entrance region - was not considered. This problem is, however, of central importance because, as even remarked by Reynolds (1883), the pipe inlet disturbances have a significant effect on the stability and laminar-turbulent transition of the pipe-entrance flow. By controlling the disturbance level at the pipe inlet, the flow studied by Reynolds (1883) was maintained laminar up to Reynolds numbers ranging from 2000 to 13 000. This number was further increased to 100 000 in the experiments of Pfenniger (1961).

Given the importance of the inlet perturbations, it is thus surprising that only a limited number of studies exist on this problem. In the experiments of Sarpkaya (1975), disturbances were introduced on the surface of the pipe entrance, and the occurrence of instability was confirmed. The reported critical Reynolds number was much lower than that estimated by theoretical studies, which may be ascribed to the finite-amplitude disturbances induced in the entrance flow. The dynamics of localised turbulence, i.e. puffs and slugs, was studied in the experimental work of Wygnanski & Champagne (1973), where the disturbances were introduced at the pipe inlet using a honeycomb, an orifice plate and a circular disk. Wygnanski *et al.* (1975) further investigated the propagation of turbulent puffs initiated by an impulsive disturbance at the entrance region. The experimental study of Zanoun *et al.* (2009) focused

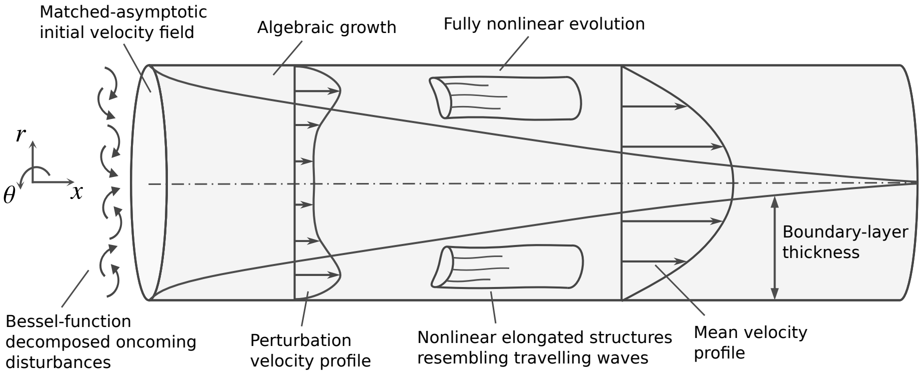

Figure 1: Schematic of the entrance region of a pipe (not to scale).

on the effect of the inlet flow conditions on the flow transition in pipe and channel flows. Different transition Reynolds numbers were measured at different streamwise positions.

Direct numerical simulations were conducted by Wu *et al.* (2015) and Wu *et al.* (2020) to investigate the flow transition to fully developed turbulence triggered by localised inlet disturbances. In Wu *et al.* (2015), the fully developed parabolic laminar velocity profile was chosen as the inlet base flow in most cases, and the plug flow was utilised in one case. The most intense inlet disturbances required to trigger transition pertained to the latter case.

Under the small-amplitude assumption, Ricco & Alvarenga (2022) performed the first theoretical study of the entrainment of free-stream vortical disturbances in the pipe entrance. Their interest was in how these disturbances are affected by the pipe confinement, and on how they grow and develop downstream. The perturbation flow at the pipe inlet was obtained by a matched asymptotic composite solution between a Bessel function vortical flow in the pipe core and a boundary-layer flow near the pipe wall. A streamwise-elongated streaky flow formed within the base-flow boundary layer and evolved towards the pipe centreline farther downstream. A good agreement between the computed velocity profiles and the available experimental data was found when the measured free-stream disturbances were weak.

1.3. *Objectives*

We investigate the entrainment of flow disturbances into the entrance of a circular pipe, and the downstream growth and evolution of the induced nonlinear vortical disturbances along the entrance region. The oncoming disturbances are physically realistic, i.e. they can be generated at the pipe inlet in a laboratory. The nonlinear boundary-region equations are derived in the cylindrical geometry for the first time, and solved numerically by marching downstream. Our study is the nonlinear extension of Ricco & Alvarenga (2022), and the first theoretical study of the entrainment and downstream evolution of finite-amplitude disturbances in the entrance region of a circular pipe.

In §2, the scaling and assumptions are presented, together with the mathematical formulation and numerical procedures. Numerical results are discussed in §3. A summary and conclusions are given in §4.

2. Mathematical formulation and numerical procedures

We consider a circular pipe of radius R^* described by a cylindrical coordinate system $\{x^*, r^*, \theta\}$, where x^* and r^* are the streamwise and radial directions, and θ is the azimuthal angle. The pipe inlet is located at $x^* = 0$, while the pipe axis and the pipe wall are at $r^* = 0$

and $r^* = R^*$, respectively. The superscript * refers to dimensional quantities hereafter. A schematic of the flow is shown in figure 1.

A pressure-driven incompressible flow is assumed to enter the pipe with a uniform velocity U^*_∞ at $x^* = 0$. Superimposed on the oncoming flow are small-amplitude gust-type vortical fluctuations that can be modelled by a Fourier–Bessel series with Fourier expansions in x^*, θ and time t^*, and a Bessel expansion in r^*. A pair of vortical modes with the same frequency f^* (and hence the same streamwise wavenumber k^*_x), but opposite azimuthal wavenumbers $\pm m_0$, is considered ($m_0 \geqslant 0$ is taken without losing generality). The circumferential wavelength of the free-stream gust at the pipe radius, $\lambda^* = 2\pi R^*/m_0$, is chosen as the reference length. The velocities and time are normalised by U^*_∞ and λ^*/U^*_∞, respectively, while the pressure p^* is normalised by $\rho^* U^{*2}_\infty$, where ρ^* is the density of the fluid.

Following Ricco & Alvarenga (2022), a single pair of free-stream gusts is passively advected by U^*_∞ and expressed as

$$\boldsymbol{u} - \{1, 0, 0\} = \epsilon \left\{ \hat{\boldsymbol{u}}^\infty_{+,\boldsymbol{m_0}} e^{i m_0 \theta} + \hat{\boldsymbol{u}}^\infty_{-,\boldsymbol{m_0}} e^{-i m_0 \theta} \right\} e^{i k_x (x-t)} + \text{c.c.}, \tag{2.1}$$

where

$$\hat{\boldsymbol{u}}^\infty_{\pm,\boldsymbol{m_0}}(r; l) = \left\{ \hat{u}^\infty_{m_0} J_{m_0}(r_0), \frac{\hat{v}^\infty_{m_0} J_{m_0}(r_0)}{r_0}, \frac{\mp i \hat{w}^\infty_{m_0} J'_{m_0}(r_0)}{\xi_{m_0,l}} \right\} = O(1). \tag{2.2}$$

Here, $\boldsymbol{u} = \{u, v, w\}$ corresponds to the velocity components in the x, r and θ directions, $\epsilon \ll 1$ is a measure of the amplitude of the disturbances, the quantities $\{\hat{u}^\infty_{m_0}, \hat{v}^\infty_{m_0}, \hat{w}^\infty_{m_0}\} = O(1)$ are complex, J_{m_0} is the Bessel function of the first kind of order m_0, $r_0 = r \xi_{m_0,l}/2R$ with $\xi_{m_0,l}$ being the lth zero of the Bessel function J_{m_0}, and c.c. denotes the complex conjugate. The notations m_0 and r_0 correspond to m and $\bar{r}$ in Ricco & Alvarenga (2022). A similar expansion of the free-stream vortical disturbances has been used in Ricco *et al.* (2011) and Marensi *et al.* (2017) for flat-plate boundary layers, Marensi & Ricco (2017) for concave boundary layers, and Ricco & Alvarenga (2021) for a channel flow. The expansion (2.1)–(2.2) is a model of free-stream vortical disturbances that could be realised in a laboratory by a grid of vibrating ribbons, a polar equivalent of the careful receptivity studies of Dietz (1999) and Borodulin *et al.* (2021).

Our focus is on oncoming disturbances with a long streamwise wavelength (i.e. low frequency), i.e. $k_x \ll 1$, which have been experimentally demonstrated to be the most likely to penetrate into a boundary layer and form streamwise-elongated structures (Matsubara & Alfredsson 2001). Under the low-frequency assumption, the continuity equation of the gust disturbances becomes

$$\xi_{m_0,l} \hat{v}^\infty_{m_0} + m_0 \hat{w}^\infty_{m_0} = 0, \tag{2.3}$$

where $\partial u/\partial x = O(k_x) \ll 1$ has been neglected.

As the oncoming flow enters the pipe, a boundary layer develops on the pipe wall. As the flow evolves downstream, the boundary-layer thickness becomes comparable with the azimuthal wavelength λ^* at $x = O(Re_\lambda)$, where $Re_\lambda = U^*_\infty \lambda^*/\nu^* \gg 1$, and ν^* is the kinematic viscosity of the fluid. A distinguished scaling is $k_x = O\left(Re_\lambda^{-1}\right)$, and the two slow variables scaled by k_x are $\bar{t} = k_x t = O(1)$ and $\bar{x} = k_x x = O(1)$. In this region, viscous–diffusion effects in the radial and azimuthal directions are comparable. The flow can be described by the nonlinear boundary-region equations (Ricco *et al.* 2011), written and solved herein in cylindrical coordinates for the first time. The linear counterpart of these equations, obtained for the turbulent Reynolds number $r_t = \epsilon Re_\lambda \ll 1$, was derived and solved in Ricco & Alvarenga (2022) for studying the growth of small-amplitude disturbances. The current research relaxes the linear assumption because $r_t = O(1)$. Nonlinear interactions are thus taken into account.

2.1. *Governing equations*

The boundary-region equations are derived from the incompressible Navier-Stokes equations

$$\nabla \cdot \boldsymbol{u} = 0, \tag{2.4}$$

$$\frac{\partial \boldsymbol{u}}{\partial t} + (\boldsymbol{u} \cdot \nabla)\boldsymbol{u} = -\nabla p + \frac{1}{Re_\lambda}\nabla^2 u. \tag{2.5}$$

The velocity $\boldsymbol{u}$ and the pressure p are decomposed into the laminar base flow and the perturbation flow, namely

$$\begin{aligned}\{\boldsymbol{u}, p\} &= \{\boldsymbol{U}, P\} + \{\tilde{\boldsymbol{u}}, \tilde{p}\} \\ &= \{U(\bar{x}, r), k_x V(\bar{x}, r), 0, P(\bar{x})\} + r_t \left\{\bar{u}, k_x \bar{v}, k_x \bar{w}, \frac{k_x}{Re_\lambda}\bar{p} + \Gamma(\bar{x})\right\},\end{aligned} \tag{2.6}$$

where the perturbation flow is expressed as a Fourier series in θ and t:

$$\{\bar{u}, \bar{v}, \bar{w}, \bar{p}, \Gamma\} = \sum_{m,n=-\infty}^{\infty} \{\hat{u}_{m,n}, \hat{v}_{m,n}, \hat{w}_{m,n}, \hat{p}_{m,n}, \hat{\Gamma}_{m,n}\} e^{im\theta + in\bar{t}}. \tag{2.7}$$

The pressure correction $\Gamma(\bar{x})$ ensures that the mass flow rate is conserved at each streamwise location and time instant as the modes $\hat{u}_{0,n}$ are generated by the nonlinear interactions. Therefore, $\hat{\Gamma}_{m,n} \neq 0$ only if $m = 0$. As the physical quantities are real, the Hermitian property applies, i.e.

$$(\hat{q}_{m,n})_{\text{c.c.}} = \hat{q}_{-m,-n}, \tag{2.8}$$

where $\hat{q}_{m,n}$ represents any Fourier coefficient $\{\hat{u}_{m,n}, \hat{v}_{m,n}, \hat{w}_{m,n}, \hat{p}_{m,n}, \hat{\Gamma}_{m,n}\}$ in (2.7).

Substituting (2.6) and (2.7) into the full Navier-Stokes equations (2.4)–(2.5), and taking the limits k_x^{-1}, $Re_\lambda \to \infty$ with $\mathcal{F} = k_x Re_\lambda = \mathcal{O}(1)$ leads to the boundary-layer equations governing the laminar base flow $\{U, V, P\}$ and to the unsteady nonlinear boundary-region equations governing the perturbation flow $\{\hat{u}_{m,n}, \hat{v}_{m,n}, \hat{w}_{m,n}, \hat{p}_{m,n}, \hat{\Gamma}_{m,n}\}$.

The laminar boundary-layer equations read (Hornbeck 1964)

$$\frac{\partial U}{\partial \bar{x}} + \frac{V}{r} + \frac{\partial V}{\partial r} = 0, \tag{2.9}$$

$$U\frac{\partial U}{\partial \bar{x}} + V\frac{\partial U}{\partial r} = -\frac{\mathrm{d}P}{\mathrm{d}\bar{x}} + \frac{1}{\mathcal{F}}\left(\frac{1}{r}\frac{\partial U}{\partial r} + \frac{\partial^2 U}{\partial r^2}\right). \tag{2.10}$$

Equation (2.9) and (2.10) are solved together with the conservation of mass flow rate at each streamwise location,

$$\int_0^R U r \mathrm{d}r = \frac{R^2}{2}, \tag{2.11}$$

and are subject to the no-slip and no-penetration conditions at the wall and the symmetry conditions at the pipe axis:

$$r = R: \quad U = V = 0, \tag{2.12}$$

$$r = 0: \quad \frac{\partial U}{\partial r} = 0, \ V = 0. \tag{2.13}$$

The initial condition is obtained by a matched asymptotic combination of the Blasius flow near the pipe wall and an inviscid flow around the pipe core (Ricco & Alvarenga 2022),

$$
\begin{aligned}
U(x,r) =& \frac{\mathrm{d}F}{\mathrm{d}\eta} - \frac{\beta i^{1/2}}{2\sqrt{2\pi}Re_\lambda^{1/2}} \int_{-\infty+i\gamma}^{+\infty+i\gamma} \frac{e^{i\zeta x}}{\zeta^{1/2} I_1(\zeta R)} \left[\frac{I_1(\zeta r)}{\zeta r} + I_1'(\zeta r)\right] \mathrm{d}\zeta + \\
& \frac{\beta i^{1/2}}{2\sqrt{2\pi}Re_\lambda^{1/2}} \int_{-\infty+i\gamma}^{+\infty+i\gamma} \frac{e^{i\zeta x}}{\zeta^{1/2}} \left[\frac{I_1'(\zeta R)}{I_1(\zeta R)} + \frac{1}{\zeta R}\right] \mathrm{d}\zeta, \quad x \ll 1
\end{aligned}
\tag{2.14}
$$

where $\eta = (R-r)(Re_\lambda/2x)^{1/2}$, F satisfies the Blasius equation $F''' + FF'' = 0$, the prime denotes differentiation, $\beta = \lim_{\eta\to\infty}(\eta - F) = 1.217\ldots$, I_1 is the modified Bessel function of the first kind, and $\gamma \in \mathbb{R} < 0$. Equations (2.9)–(2.11), supplemented by conditions (2.12)–(2.14), are solved by an improved version of the numerical scheme of Hornbeck (1964). A detailed description of the numerical procedure is provided in the supplementary material S1 of Ricco & Alvarenga (2022). The numerical results are discussed in §4.1 of Ricco & Alvarenga (2022).

The perturbation-flow unsteady nonlinear boundary-region equations are as follows. The continuity equation is

$$
\frac{\partial \hat{u}_{m,n}}{\partial \bar{x}} + \frac{\hat{v}_{m,n}}{r} + \frac{\partial \hat{v}_{m,n}}{\partial r} + \frac{im}{r}\hat{w}_{m,n} = 0. \tag{2.15}
$$

The x-momentum equation is

$$
\begin{aligned}
&\left(in + \frac{\partial U}{\partial \bar{x}} + \frac{m^2}{\mathcal{F}r^2}\right)\hat{u}_{m,n} + U\frac{\partial \hat{u}_{m,n}}{\partial \bar{x}} + \left(V - \frac{1}{\mathcal{F}r}\right)\frac{\partial \hat{u}_{m,n}}{\partial r} + \hat{v}_{m,n}\frac{\partial U}{\partial r} - \\
&\frac{1}{\mathcal{F}}\frac{\partial^2 \hat{u}_{m,n}}{\partial r^2} + \frac{\mathrm{d}\hat{\Gamma}_{0,n}}{\mathrm{d}\bar{x}} = r_t \hat{\mathcal{X}}_{m,n}.
\end{aligned}
\tag{2.16}
$$

The r-momentum equation is

$$
\begin{aligned}
&\left(in + \frac{\partial V}{\partial r} + \frac{m^2+1}{\mathcal{F}r^2}\right)\hat{v}_{m,n} + U\frac{\partial \hat{v}_{m,n}}{\partial \bar{x}} + \hat{u}_{m,n}\frac{\partial V}{\partial \bar{x}} + \left(V - \frac{1}{\mathcal{F}r}\right)\frac{\partial \hat{v}_{m,n}}{\partial r} + \\
&\frac{1}{\mathcal{F}}\frac{\partial \hat{p}_{m,n}}{\partial r} - \frac{1}{\mathcal{F}}\frac{\partial^2 \hat{v}_{m,n}}{\partial r^2} + \frac{2im}{\mathcal{F}r^2}\hat{w}_{m,n} = r_t \hat{\mathcal{Y}}_{m,n}.
\end{aligned}
\tag{2.17}
$$

The θ-momentum equation is

$$
\begin{aligned}
&\left(in + \frac{V}{r} + \frac{m^2+1}{\mathcal{F}r^2}\right)\hat{w}_{m,n} + U\frac{\partial \hat{w}_{m,n}}{\partial \bar{x}} + \left(V - \frac{1}{\mathcal{F}r}\right)\frac{\partial \hat{w}_{m,n}}{\partial r} + \frac{im}{\mathcal{F}r}\hat{p}_{m,n} - \\
&\frac{1}{\mathcal{F}}\frac{\partial^2 \hat{w}_{m,n}}{\partial r^2} - \frac{2im}{\mathcal{F}r^2}\hat{v}_{m,n} = r_t \hat{\mathcal{Z}}_{m,n}.
\end{aligned}
\tag{2.18}
$$

The right-hand sides of the momentum equations (2.16)–(2.18) denote the nonlinear terms

$$
\left.
\begin{aligned}
\hat{\mathcal{X}}_{m,n} &= -\left(\frac{\partial \widehat{\bar{u}\bar{u}}}{\partial \bar{x}} + \frac{\partial \widehat{\bar{u}\bar{v}}}{\partial r} + \frac{\widehat{\bar{u}\bar{v}} + im\widehat{\bar{u}\bar{w}}}{r}\right)_{m,n}, \\
\hat{\mathcal{Y}}_{m,n} &= -\left(\frac{\partial \widehat{\bar{u}\bar{v}}}{\partial \bar{x}} + \frac{\partial \widehat{\bar{v}\bar{v}}}{\partial r} + \frac{\widehat{\bar{v}\bar{v}} + im\widehat{\bar{v}\bar{w}} - \widehat{\bar{w}\bar{w}}}{r}\right)_{m,n}, \\
\hat{\mathcal{Z}}_{m,n} &= -\left(\frac{\partial \widehat{\bar{u}\bar{w}}}{\partial \bar{x}} + \frac{\partial \widehat{\bar{v}\bar{w}}}{\partial r} + \frac{im\widehat{\bar{w}\bar{w}}}{r} + \frac{2\widehat{\bar{v}\bar{w}}}{r}\right)_{m,n},
\end{aligned}
\right\}
\tag{2.19}
$$

where $\hat{}$ indicates Fourier transformed quantities. In the limit $r_t \ll 1$, the linearised boundary-region equations of Ricco & Alvarenga (2022) are recovered. The pressure correction $\hat{\Gamma}_{0,n}$ becomes a further unknown variable for $m = 0$, and one more condition is thus required to solve the system. Analogous to (2.11) for the base-flow problem, this condition is the conservation of mass flow rate at each instant in time and at each streamwise location. As discussed in Appendix A, this condition is expressed as

$$\int_0^R \hat{u}_{0,n} r \mathrm{d}r = 0. \tag{2.20}$$

Since the partial differential system (2.15)–(2.20) is parabolic in the streamwise direction and elliptic in the radial and azimuthal directions, appropriate initial and boundary conditions are needed. These conditions are presented in §2.2. Further treatment of (2.15)–(2.20) is carried out in §2.3 for different values of m. The numerical procedures are discussed in §2.4.

2.2. *Initial and boundary conditions*

While the streamwise velocity of the induced disturbances acquires an order-one amplitude at $\bar{x} = O(1)$, the velocity fluctuations near the pipe inlet are of small amplitude $O(\epsilon)$ and nonlinear effects can therefore be neglected there. Hence the initial conditions derived by Ricco & Alvarenga (2022) can be used. Comparison of the velocity expansions (2.6) here and (2.6) in Ricco & Alvarenga (2022) leads to the relations

$$\left\{\hat{u}_{m_0,-1}, \hat{v}_{m_0,-1}\right\} = \frac{1}{Re_\lambda}\left\{\frac{im_0}{k_x}\bar{u}_x + \bar{u}_x^{(0)}, \frac{im_0}{k_x}\bar{u}_r + \bar{u}_r^{(0)}\right\}, \tag{2.21}$$

where $\bar{u}_x$, $\bar{u}_r$, $\bar{u}_x^{(0)}$ and $\bar{u}_r^{(0)}$ are given by the analytical expressions (3.25)–(3.27) and (3.32) in Ricco & Alvarenga (2022). The azimuthal velocity $\hat{w}_{m_0,-1}$ can be found through the continuity equation (2.15), with $\hat{u}_{m_0,-1}$ and $\hat{v}_{m_0,-1}$ given by (2.21). For the opposite wavenumber $m = -m_0$, the same streamwise and radial components but opposite azimuthal component are derived

$$\left\{\hat{u}_{-m_0,-1}, \hat{v}_{-m_0,-1}, \hat{w}_{-m_0,-1}\right\} = \left\{\hat{u}_{m_0,-1}, \hat{v}_{m_0,-1}, -\hat{w}_{m_0,-1}\right\}. \tag{2.22}$$

It also occurs that

$$\hat{u}_{m,n} = \hat{v}_{m,n} = \hat{w}_{m,n} = 0 \quad \text{for} \;\; (m,n) \neq (\pm m_0, -1). \tag{2.23}$$

Since the streamwise derivative of $\hat{p}_{m,n}$ is negligible in the x-momentum equation (2.16) under the low-frequency assumption, no initial condition for $\hat{p}_{m,n}$ is required.

In the radial direction, equations (2.15)–(2.20) are subjected to the no-slip and no-penetration conditions at the wall ($r = R$),

$$\hat{u}_{m,n} = \hat{v}_{m,n} = \hat{w}_{m,n} = 0, \tag{2.24}$$

while the boundary conditions at the pipe axis ($r = 0$) are

$$\left.\begin{array}{llllll} \hat{u}'_{m,n} = 0, & \hat{v}_{m,n} = 0, & \hat{w}_{m,n} = 0, & \hat{p}'_{m,n} = 0, & \text{for} & m = 0, \\ \hat{u}_{m,n} = 0, & \hat{v}'_{m,n} = 0, & \hat{w}'_{m,n} = 0, & \hat{p}_{m,n} = 0, & \text{for} & |m| = 1, \\ \hat{u}_{m,n} = 0, & \hat{v}_{m,n} = 0, & \hat{w}_{m,n} = 0, & \hat{p}_{m,n} = 0, & \text{for} & |m| \geqslant 2, \end{array}\right\} \tag{2.25}$$

where the prime indicates the derivative with respect to r. Conditions (2.25) are derived following Batchelor & Gill (1962), Tuckerman (1989) and Lewis & Bellan (1990), who studied the physical constraints on the coefficients of Fourier expansions in cylindrical coordinates (refer also to supplementary material S3 of Ricco & Alvarenga (2022)).

2.3. *Initial-boundary value problems*

For convenience of the numerical calculations, the nonlinear boundary-region equations (2.15)–(2.20), together with the initial conditions (2.21)–(2.23) and the boundary conditions (2.24)–(2.25), are solved in different forms according to the value of m.

Case I For the components with $m \neq 0$, the pressure $\hat{p}_{m,n}$ and the azimuthal velocity $\hat{w}_{m,n}$ can be eliminated from (2.15)–(2.19) as in Ricco & Alvarenga (2022). The resulting equations read

$$\left(in + \frac{\partial U}{\partial \bar{x}} + \frac{m^2}{\mathcal{F} r^2}\right)\hat{u}_{m,n} + \left(V - \frac{1}{\mathcal{F} r}\right)\frac{\partial \hat{u}_{m,n}}{\partial r} + U\frac{\partial \hat{u}_{m,n}}{\partial \bar{x}} - \frac{1}{\mathcal{F}}\frac{\partial^2 \hat{u}_{m,n}}{\partial r^2} + \frac{\partial U}{\partial r}\hat{v}_{m,n} = r_t \hat{\mathcal{X}}_{m,n}, \tag{2.26}$$

$$\begin{aligned}
&\widehat{V}\hat{v}_{m,n} + \widehat{V}_r\frac{\partial \hat{v}_{m,n}}{\partial r} + \widehat{V}_x\frac{\partial \hat{v}_{m,n}}{\partial \bar{x}} + \widehat{V}_{rr}\frac{\partial^2 \hat{v}_{m,n}}{\partial r^2} + \widehat{V}_{xr}\frac{\partial^2 \hat{v}_{m,n}}{\partial \bar{x}\partial r} + \widehat{V}_{rrr}\frac{\partial^3 \hat{v}_{m,n}}{\partial r^3} + \widehat{V}_{xrr}\frac{\partial^3 \hat{v}_{m,n}}{\partial \bar{x}\partial r^2} + \\
&\widehat{V}_{rrrr}\frac{\partial^4 \hat{v}_{m,n}}{\partial r^4} + \hat{U}\hat{u}_{m,n} + \widehat{U}_r\frac{\partial \hat{u}_{m,n}}{\partial r} + \widehat{U}_x\frac{\partial \hat{u}_{m,n}}{\partial \bar{x}} + \widehat{U}_{rr}\frac{\partial^2 \hat{u}_{m,n}}{\partial r^2} + \widehat{U}_{xr}\frac{\partial^2 \hat{u}_{m,n}}{\partial \bar{x}\partial r} + \\
&\widehat{U}_{xrr}\frac{\partial^3 \hat{u}_{m,n}}{\partial \bar{x}\partial r^2} = r_t\frac{r^2}{m^2}\frac{\partial^2 \hat{\mathcal{X}}_{m,n}}{\partial \bar{x}\partial r} + r_t\hat{\mathcal{Y}}_{m,n} + \frac{i r_t}{m}\frac{\partial\left(r\hat{\mathcal{Z}}_{m,n}\right)}{\partial r},
\end{aligned} \tag{2.27}$$

where the coefficients $\widehat{V}, \widehat{V}_r, \widehat{V}_x, \cdots, \widehat{U}_{xrr}$ are given in Appendix B. Only the initial and boundary conditions for $\{\hat{u}_{m,n}, \hat{v}_{m,n}\}$ are needed in this case. The initial conditions are given in (2.21)–(2.23). The boundary conditions are

$$\hat{u}_{m,n} = \hat{v}_{m,n} = \hat{v}'_{m,n} = 0, \quad \text{at } r = R \tag{2.28}$$

and

$$\left.\begin{aligned}
&\hat{u}_{m,n} = 0,\ \hat{v}'_{m,n} = 0,\ \hat{v}'''_{m,n} = 0, && \text{for} \quad |m| = 1,\\
&\hat{u}_{m,n} = 0,\ \hat{v}_{m,n} = 0,\ \hat{v}''_{m,n} = 0, && \text{for} \quad |m| = 2,\\
&\hat{u}_{m,n} = 0,\ \hat{v}_{m,n} = 0,\ \hat{v}'_{m,n} = 0, && \text{for} \quad |m| > 2,
\end{aligned}\right\} \quad \text{at } r = 0. \tag{2.29}$$

At the pipe wall, $r = R$, the last condition $\hat{w}_{m,n} = 0$ in (2.24) is replaced by $\hat{v}'_{m,n} = 0$ in (2.28), which is obtained by inserting (2.24) into the continuity equation (2.15). At the pipe axis, $r = 0$, the conditions for $\hat{w}$ and $\hat{w}'$ in (2.25) for different m are replaced following the physical constraints proposed by Batchelor & Gill (1962), Khorrami *et al.* (1989), Tuckerman (1989) and Lewis & Bellan (1990), as discussed in supplementary material S3 of Ricco & Alvarenga (2022). The azimuthal velocity $\hat{w}_{m,n}$ can be obtained *a posteriori* from the continuity equation and the pressure $\hat{p}_{m,n}$ can then be calculated from either the r-momentum equation (2.17) or the θ-momentum equation (2.18).

Case II For the components with $m = 0$, the pressure $\hat{p}_{0,n}$ appears only in the r-momentum equation (2.17). The three velocity components $\{\hat{u}_{0,n}, \hat{v}_{0,n}, \hat{w}_{0,n}\}$ can be solved by the continuity, x- and θ-momentum equations,

$$\frac{\partial \hat{u}_{0,n}}{\partial \bar{x}} + \frac{\hat{v}_{0,n}}{r} + \frac{\partial \hat{v}_{0,n}}{\partial r} = 0, \tag{2.30}$$

$$\left(in + \frac{\partial U}{\partial \bar{x}}\right)\hat{u}_{0,n} + U\frac{\partial \hat{u}_{0,n}}{\partial \bar{x}} + \left(V - \frac{1}{\mathcal{F} r}\right)\frac{\partial \hat{u}_{0,n}}{\partial r} + \hat{v}_{0,n}\frac{\partial U}{\partial r} - \frac{1}{\mathcal{F}}\frac{\partial^2 \hat{u}_{0,n}}{\partial r^2} + \frac{\mathrm{d}\hat{\Gamma}_{0,n}}{\mathrm{d}\bar{x}} = r_t\hat{\mathcal{X}}_{0,n}, \tag{2.31}$$

$$\left(in + \frac{V}{r} + \frac{1}{\mathcal{F} r^2}\right)\hat{w}_{0,n} + U\frac{\partial \hat{w}_{0,n}}{\partial \bar{x}} + \left(V - \frac{1}{\mathcal{F} r}\right)\frac{\partial \hat{w}_{0,n}}{\partial r} - \frac{1}{\mathcal{F}}\frac{\partial^2 \hat{w}_{0,n}}{\partial r^2} = r_t\hat{\mathcal{Z}}_{0,n}, \tag{2.32}$$

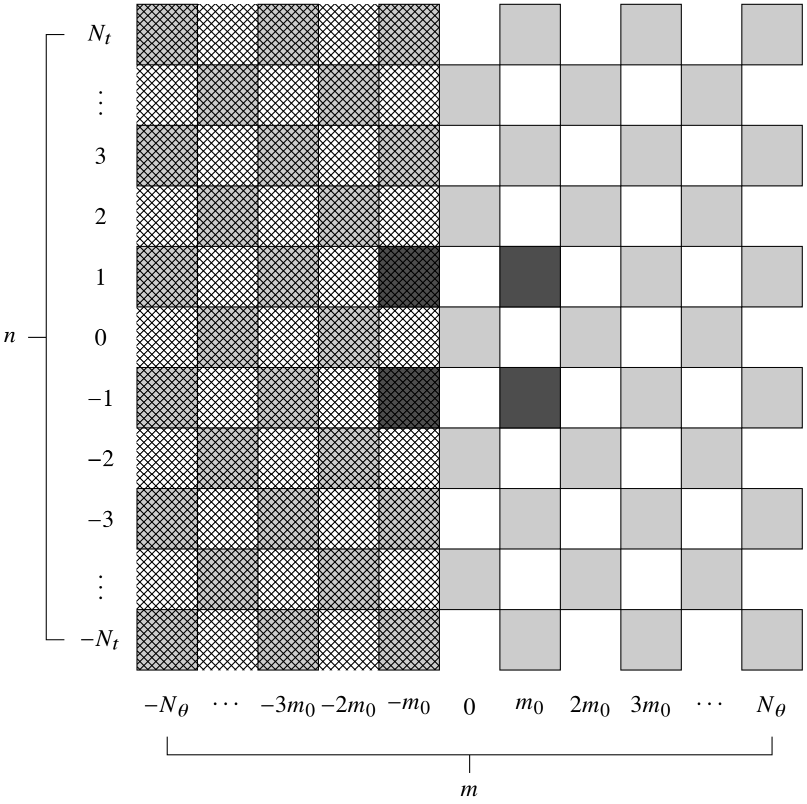

Figure 2: Sketch of Fourier modes induced by a pair of free-stream vortical modes. Dark grey squares: forcing modes $(\pm m_0, \pm 1)$. Light grey squares: nonlinearly generated modes. The modes in the shaded area are computed through the Hermitian property (2.8).

together with (2.20) for the conservation of the mass flow rate, as discussed in §2.1. The pressure $\hat{p}_{0,n}$ is computed *a posteriori* by integrating the r-momentum equation (2.17). The boundary conditions for the velocity components and the pressure are given in (2.24) and (2.25) for $m = 0$. The initial conditions for $\hat{u}_{0,n}, \hat{v}_{0,n}, \hat{w}_{0,n}$ are null.

2.4. *Numerical procedures*

The initial-boundary value problems are solved by marching in the streamwise direction $\bar{x}$. The governing equations for both cases are discretised by second-order finite-difference schemes employing a one-sided backward uniform grid along $\bar{x}$ and a central-difference uniform grid along r. The discretised system of case I forms a block tridiagonal matrix and is solved at each $\bar{x}$ location by a standard block tridiagonal matrix algorithm (Cebeci 2002). For case II, the composite trapezoidal rule is used for the calculation of the integral (2.20). Since the velocity components and the pressure gradient are computed simultaneously, the block tridiagonal structure of the matrix is lost. A novel modified block tridiagonal matrix algorithm is utilised to accelerate the numerical solution of this system, as discussed in Appendix C.

The computation of the nonlinear terms on the right-hand sides of the momentum equations is refined by a predictor–corrector method at each $\bar{x}$ location. In the predictor step, the initial approximation of the nonlinear terms uses the results at the previous $\bar{x}$ location to treat the discretised nonlinear system explicitly. The velocity computed from the predictor step is used to improve the initial guess in the corrector step. This iteration is repeated until a convergence criterion is fulfilled. An under-relaxation method is used to accelerate this procedure. At each iteration, nonlinear terms are calculated using the pseudo-spectral method, in which first the Fourier coefficients of the velocity components are transformed to the physical space to carry out the multiplications, and the products are then transformed back to the spectral space. The aliasing error is eliminated by employing the $3/2$ rule, which avoids the spurious energy cascade from the unresolved high-frequency modes into the resolved low-frequency ones. As the Hermitian property is applied for the azimuthal angle θ, only the Fourier modes with non-negative indices m need to be calculated. The modes with negative m indices are evaluated through (2.8). Figure 2 shows a sketch of the Fourier modes induced by a pair of free-steam vortical modes $(\pm m_0, \pm 1)$. Only the modes with $m = \pm m_0, \pm 2m_0, \pm 3m_0, \cdots$ and $n = \pm 1, \pm 2, \pm 3, \cdots$ can be generated by nonlinearity. Fourier modes are truncated at $m = \pm N_\theta$ and $n = \pm N_t$ for the azimuthal wavenumber and the frequency, respectively. Resolution checks show that the use of $N_t = 6$, $N_\theta = 12$ is sufficient to capture the nonlinear effects induced by the free-stream forcing modes with wavenumber $m_0 = 2$. For larger m_0, a correspondingly larger value of N_θ is necessary (e.g. $N_\theta = 18$ for $m_0 = 3$).

3. Results

In the analysis of the flow, the kinetic energy of the free-stream gust averaged over the pipe cross-section is kept constant:

$$\begin{aligned}\mathcal{E}^{gust}_{m_0,l} &= \frac{1}{2\pi R^2}\int_0^{2\pi}\int_0^R \left(|\tilde{u}|^2 + |\tilde{v}|^2 + |\tilde{w}|^2\right) r\mathrm{d}r\mathrm{d}\theta \\ &= \frac{4\epsilon^2}{R^2}\int_0^R \left[\left(\hat{u}^{\infty}_{m_0} J_{m_0}(r_0)\right)^2 + \left(\frac{\hat{v}^{\infty}_{m_0} J_{m_0}(r_0)}{r_0}\right)^2 + \left(\frac{\hat{v}^{\infty}_{m_0} J'_{m_0}(r_0)}{m_0}\right)^2\right] r\mathrm{d}r, \end{aligned} \tag{3.1}$$

where the gust velocity components in (2.2) have been used. The relation (2.3) is utilised to eliminate $\hat{w}^{\infty}_{m_0}$ from (3.1). Without losing generality, $\hat{u}^{\infty}_{m_0}$ is fixed at 1 in our analysis. With m_0 and l specified, the only parameter to be determined is $\hat{v}^{\infty}_{m_0}$, which is found by equating $\mathcal{E}^{gust}_{m_0,l}$ to $\mathcal{E}^{gust}_{1,1}$, the perturbation energy for $m_0 = l = 1$ and $\hat{v}^{\infty}_{m_0} = 1$. A similar approach was adopted in Schmid & Henningson (1994), where the maximum energy amplification was computed over initial conditions with the same energy norm. The intensity used to measure the fluctuation level of the gust is defined as $Tu = \sqrt{(2/3)\mathcal{E}^{gust}_{m_0,l}}$.

In §2, the circumferential wavelength of the gust λ^* at the pipe radius is selected as the reference length in order to relate our asymptotic analysis to the boundary-layer analysis of Leib *et al.* (1999), while the numerical results are presented herein with quantities rescaled by the pipe radius R^*, i.e. $\boldsymbol{u} = \boldsymbol{u}(x_R, r_R; k_{x,R}, Re_R, l, m_0)$, where $x_R = x^*/R^*$, $r_R = r^*/R^*$, $k_{x,R} = k^*_x R^*$ and $Re_R = U^*_\infty R^*/\nu^*$. We focus on the nonlinear evolution of disturbances in the parameter space $k_{x,R} \ll 1$ and $Re_R < 10000$, where Tollmien–Schlichting waves are not present (refer to figure 2 of Ricco & Alvarenga (2022)). In our reference case, $k_{x,R} = 0.02$, $Re_R = 1000$, $l = 3$, $m_0 = 2$ and $\epsilon = 0.05$ (i.e. $Tu \approx 4\%$).

The intensity of the disturbances is monitored by the root mean square (r.m.s.) of the streamwise velocity fluctuation, u_{rms} (Pope 2000, p.687):

$$u_{rms} = r_t\left(\sum_{m=-N_\theta}^{N_\theta}\sum_{n=-N_t}^{N_t}\left|\hat{u}_{m,n}\right|^2\right)^{1/2}, \quad n \neq 0. \tag{3.2}$$

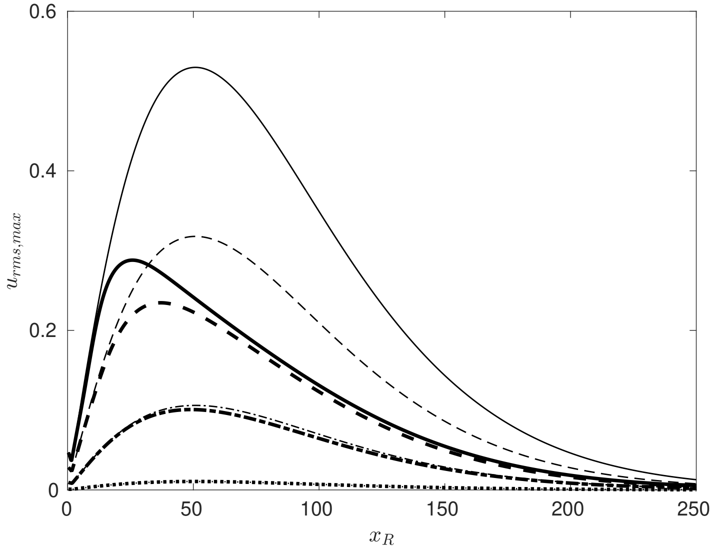

Figure 3: Thick lines: nonlinear streamwise development of $u_{rms,max}$ for $\epsilon = 0.001$ (dotted), 0.01 (dash-dotted), 0.03 (dashed), 0.05 (solid). Thin lines: linear solutions rescaled by corresponding ϵ value.

3.1. *Effect of flow parameters*

Figure 3 shows the nonlinear streamwise development of the maximum u_{rms} (thick lines), i.e. $u_{rms,max} = \max_{r_R} u_{rms}$, for different values of $\epsilon = 0.001, 0.01, 0.03, 0.05$ (i.e. $Tu \approx 0.08\%, 0.8\%, 2.4\%, 4\%$). The linear results are rescaled by the corresponding ϵ value and displayed by thin lines. The linear and nonlinear solutions overlap when the amplitude of the oncoming disturbance is small ($\epsilon = 0.001$) due to the weak nonlinear interaction, while nonlinear effects become more intense as ϵ increases. When $\epsilon = 0.03$ and 0.05, the nonlinear growth of the disturbances agrees with the corresponding linear growth only near the pipe inlet, and becomes much slower farther downstream. The peak location of the nonlinear profiles moves upstream as ϵ increases, and the peak amplitude is lower than the corresponding linear one. This latter result indicates the stabilising role of nonlinearity and the overprediction of the linear results. The maximum amplification of the nonlinear solution for $\epsilon = 0.05$ is, for example, only 54.4% of that of the linear solution. Sufficiently downstream, both linear and nonlinear disturbances experience monotonic decay and tend to zero. The stabilising effect of nonlinearity has already been noticed, for example, by Ricco *et al.* (2011) and Marensi & Ricco (2017) for the development of the streaks in boundary layers over flat and concave plates, respectively.

Figure 4 shows the effects of different parameters, $k_{x,R}$, Re_R, l and m_0, on the nonlinear development of $u_{rms,max}$ along the streamwise direction x_R. In figure 4(a), the overlap of profiles at the smaller x_R indicates that the streamwise wavenumber $k_{x,R}$ has no influence on the initial growth of the disturbances. The profiles for $k_{x,R} = 0.001$ and 0.02 are almost indistinguishable for the whole extent x_R of the pipe. By further increasing $k_{x,R}$ up to 0.1, the amplitude of $u_{rms,max}$ reaches a lower peak and decays at a larger rate.

Figure 4(b) displays the influence of the Reynolds number Re_R ranging from 1000 to 2500. The independence of the initial growth of the disturbance is also found by changing Re_R. For $Re_R \leqslant 2000$, the evolution features one maximum after the initial growth, while, for $Re_R > 2000$, two maxima are observed. Farther downstream, the disturbance decays at a slower rate as Re_R increases.

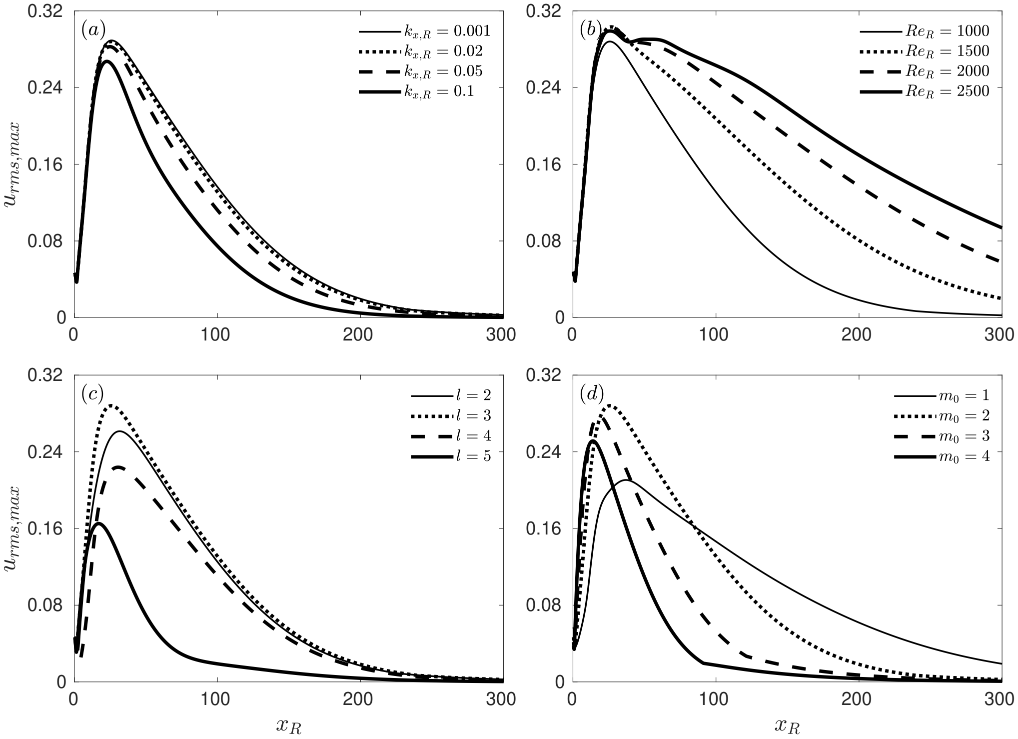

Figure 4: Effects of different parameters on the streamwise development of $u_{rms,max}$. (a) Streamwise wavenumber $k_{x,R}$; (b) Reynolds number Re_R; (c) parameter l characterising the radial length scale; (d) azimuthal wavenumber m_0.

Figure 4(c) shows how the change of the parameter l affects the downstream development of $u_{rms,max}$. As the characteristic radial scale of the oncoming disturbances is defined by the lth zero of the Bessel function, i.e. $\xi_{m_0,l}$ in expansion (2.1)–(2.2), a large l value corresponds to a small characteristic radial length scale, as shown in figure 20(a) of Ricco & Alvarenga (2022) The most intense growth occurs for $l = 3$.

The effect of the azimuthal wavenumber m_0 is shown in figure 4(d). Increasing m_0 induces a more intense initial growth. Different from the linear case where the maximum growth is found at wavenumber $m_0 = 3$ (Ricco & Alvarenga 2022), the nonlinear disturbances grow the most for $m_0 = 2$. A similar finding was reported by Reshotko & Tumin (2001) in the analysis of spatial transient growth in fully developed pipe flow, where non-stationary optimal disturbances were obtained for azimuthal wavenumbers larger than 1. The smaller m_0, the more the disturbances persist downstream.

3.2. *Results for a representative case*

The representative case with $k_{x,R} = 0.02$, $Re_R = 1000$, $l = 3$, $m_0 = 2$, $\epsilon = 0.05$ is analysed. Figures 5(a) and 5(b) show the profiles of u_{rms} at different streamwise locations. The maximum of u_{rms} appears close to the wall for locations near the pipe inlet, and gradually shifts towards the centreline as x_R increases. Its amplitude increases with x_R up to $x_R \approx 26$, after which a monotonic decrease occurs downstream. Near the pipe inlet, a significant disturbance growth is obtained in the region close to the pipe core ($0.1 < r_R < 0.5$) where the base flow is largely inviscid. The disturbances in boundary layers subjected to free-stream turbulence show a similar growth in the outer region (figure 2(c) of Matsubara & Alfredsson

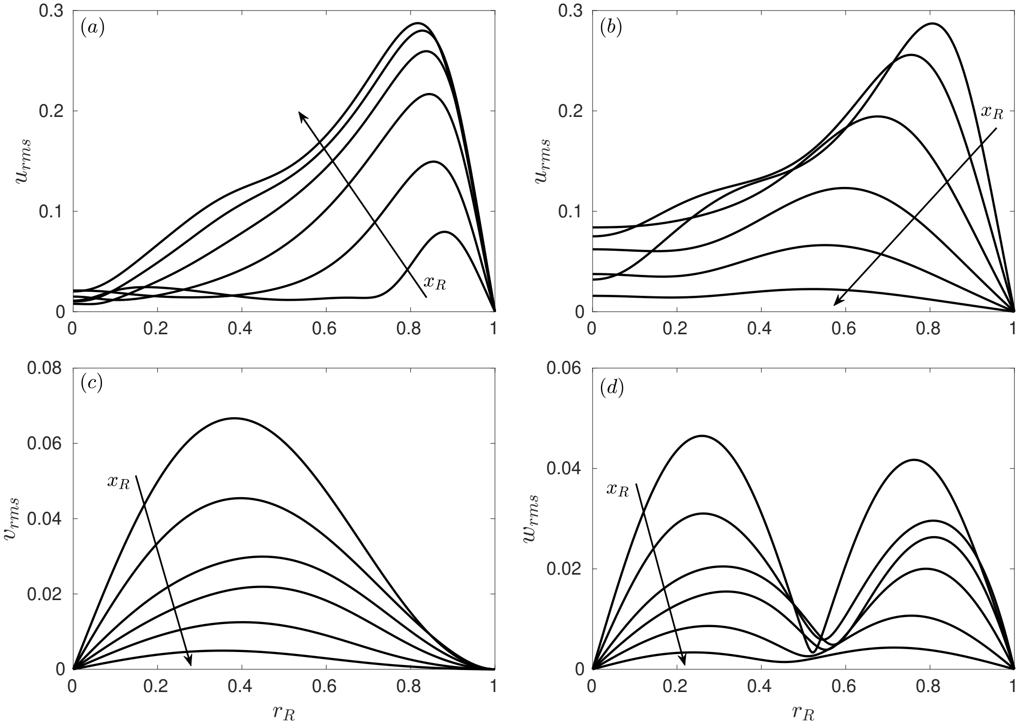

Figure 5: Profiles of u_{rms}, v_{rms} and w_{rms} at different streamwise locations: (a) growing u_{rms} at $x_R = 4, 8, 12, 16, 20, 24$; (b) decaying u_{rms} at $x_R = 28, 44, 70, 104, 140, 191$. (c, d) v_{rms} and w_{rms} at $x_R = 4, 12, 20, 28, 44, 70$. Arrows indicate the increasing x_R direction.

(2001) and figure 10 of Ricco *et al.* (2011)). This growth does not occur in the linearised case, where the disturbances are confined in the near-wall region (figure 15 of Ricco & Alvarenga (2022)). The streamwise developments of v_{rms} and w_{rms} are shown in figures 5(c) and 5(d). The amplitudes of v_{rms} and w_{rms} are comparable with that of u_{rms} close to the pipe inlet, while they become much smaller downstream after considerable attenuation.

Figure 6 displays the downstream development of the forcing mode $(m, n) = (2, 1)$ (red line) and the nonlinearly generated modes, which are characterised by $\max_{r_R} |r_t \hat{u}_{m,n}|$, the maximum intensity of $|r_t \hat{u}_{m,n}|$ at each x_R location. For the assumed free-stream disturbances (2.1), modes (m, n) and $(-m, n)$ have the same amplitude. Modes (m, n) and $(-m, -n)$ also have the same amplitude because of the Hermitian property (2.8). Therefore, without losing generality, only the results for $m \geqslant 0$ and $n \geqslant 0$ are presented. The mean-flow distortion $\hat{u}_{0,0}$ acquires considerable growth shortly downstream of the pipe inlet, overshoots the forcing mode $\hat{u}_{2,1}$ at $x_R \approx 24.4$, and becomes dominant downstream. The amplitude of the higher harmonics also grows because of the strong nonlinear interaction when $\epsilon = 0.05$, and then attenuates due to viscous effects. Downstream of $x_R = 200$, only the forcing mode $\hat{u}_{2,1}$, the mean-flow distortion $\hat{u}_{0,0}$ and the pulsatile mode $\hat{u}_{0,2}$ still exist. They all decay to zero farther downstream.

Figure 7 shows the streamwise velocity profiles of the mean-flow distortion $r_t \hat{u}_{0,0}$, the forcing modes $r_t |\hat{u}_{2,1}|$ and the higher harmonics $r_t |\hat{u}_{0,2}|$, $r_t |\hat{u}_{4,0}|$, $r_t |\hat{u}_{4,2}|$ at six different streamwise locations, $x_R = 4, 16, 32, 51, 96, 180$. The most intense growth is obtained by $\max_{r_R} |r_t \hat{u}_{0,0}|$ at $x_R = 51$ (refer to figure 6). The ordinate axis in 7(a) and 7(f) is stretched

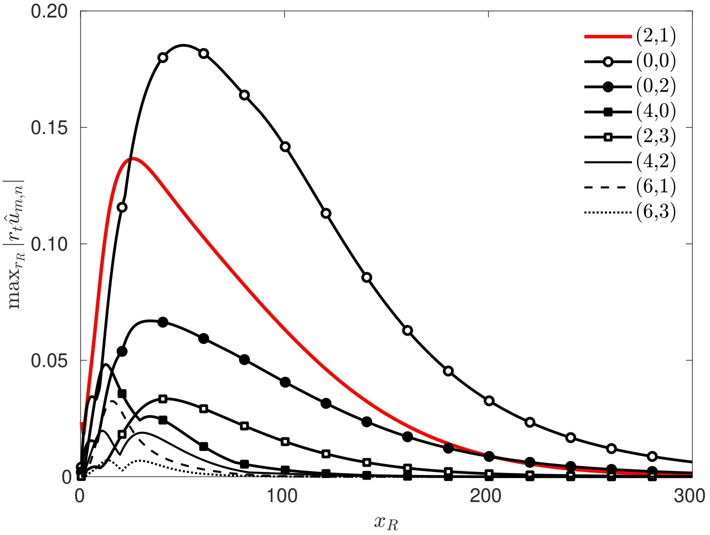

Figure 6: Streamwise development of the forcing mode (red line) and nonlinearly generated modes, characterised by $\max_{r_R}|r_t\hat{u}_{m,n}|$.

by a factor of 2 for clarity. Significant growth and decay in the velocity amplitude are observed for modes $r_t\hat{u}_{0,0}$, $r_t|\hat{u}_{2,1}|$ and $r_t|\hat{u}_{0,2}|$ along the pipe entrance. Moreover, the shape of velocity profiles changes substantially as the flow evolves downstream. The positive values of the mode $r_t\hat{u}_{0,0}$ near the wall indicate an increase of the wall-shear stress. The second harmonics, $r_t|\hat{u}_{4,0}|$ and $r_t|\hat{u}_{4,2}|$, experience considerable attenuation shortly after the initial growth and are almost negligible at $x_R = 96$ and 180.

Figure 8 shows the streamwise velocity profiles of the laminar base flow U (dashed lines) and the mean flow $\bar{U}$ (solid lines), i.e. the velocity averaged in t and θ, at the same streamwise locations as those in figure 7. Mathematically, the distorted mean flow $\bar{U}$ is the sum of the laminar base flow and the mean-flow distortion, i.e. $\bar{U} = U + r_t\hat{u}_{0,0}$. A significant deviation from the laminar base flow is observed in figure 8(d) ($x_R = 51$), where $\max_{r_R}|r_t\hat{u}_{0,0}|$ reaches the maximum growth. In the pipe core region, the profile exhibits a deficit with respect to the laminar base flow, while it is larger than the laminar value near the wall. The profiles of the mean-flow distortion $r_t\hat{u}_{0,0}$ shown in figure 7 further explain these velocity deficits and surpluses. Positive mean-flow distortion $r_t\hat{u}_{0,0}$ always exists near the pipe wall, while in the pipe core it is positive only near the inlet, and negative farther downstream.

Figure 9 displays contour plots of the velocity components $\tilde{u}$, $\tilde{v}$ and $\tilde{w}$ (from left to right) at $\bar{t} = 0$ and four different streamwise locations $x_R = 4, 26, 60, 150$ (from top to bottom). These plots visualise the formation and evolution of elongated pipe-entrance nonlinear structures (EPENS). Near the pipe inlet ($x_R = 4$), the three velocity components are of comparable amplitude. The EPENS appear because the streamwise component $\tilde{u}$ becomes prevalent at $x_R = 26$ (attributed to the growth of $\tilde{u}$ and the attenuation of $\tilde{v}$ and $\tilde{w}$), where the disturbances are most amplified, as shown in figure 3. In contrast to the nonlinear streaks observed in transitional boundary-layer flows (Matsubara & Alfredsson 2001) that are confined in the near-wall region, these EPENS occupy the entire cross-section with two high-speed streaks near the pipe wall, and two low-speed streaks near the pipe core. The twofold rotational symmetry featured by these EPENS results from the dominance of the forcing mode $\hat{u}_{2,1}$ among all the modes with $m \neq 0$ (refer to figure 6). The modes with $m = 0$ are uniform in the azimuthal direction. The gradual downstream attenuation after $x_R = 26$ can be observed

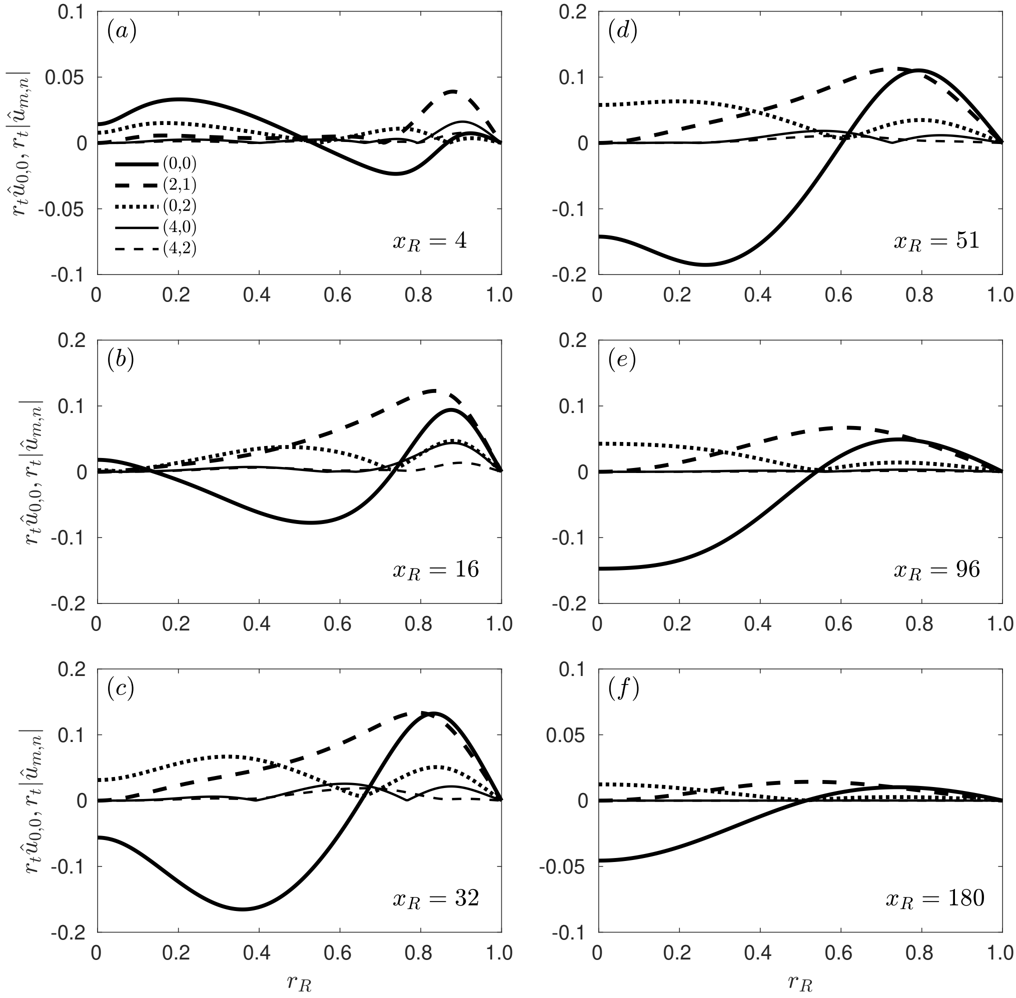

Figure 7: Streamwise velocity profiles of the mean-flow distortion $r_t\hat{u}_{0,0}$, forcing modes $r_t|\hat{u}_{2,1}|$ and second harmonics $r_t|\hat{u}_{0,2}|$, $r_t|\hat{u}_{4,0}|$, $r_t|\hat{u}_{4,2}|$ at different streamwise locations.

in the last two rows of figure 9, corresponding to $x_R = 60$ and 150. At $x_R = 60$ and 150, the low-speed streaks merge near the pipe core, flanked by the high-speed streaks on their sides. Contours of the streamwise velocity $\tilde{u}$ at $x_R = 200$ and four different time phases $\bar{t} = 0, \pi/4, \pi/2, 3\pi/4$ are shown in figure 10. The radial and azimuthal velocities $\tilde{v}$ and $\tilde{w}$ are $O(10^{-5})$ at that location, thus are not shown. The distributions of $\tilde{u}$ at $\bar{t} \in [\pi, 2\pi]$ exhibit the same features as those at $\bar{t} \in [0, \pi]$, but with a rotation of 90° around the pipe axis.

3.3. *Comparison with travelling waves*

The nonlinear vortical structures evolving along the pipe entrance are now compared with travelling waves appearing in fully developed pipe flow. Inspired by the self-sustained process proposed by Waleffe (1997), Faisst & Eckhardt (2003) and Wedin & Kerswell (2004) discovered three-dimensional travelling waves (TWs) in pipe flow. These nonlinear waves consist of streamwise vortices, streaks and streamwise-dependent wavy structures. They were also observed experimentally in turbulent puffs and in fully developed turbulence by Hof *et al.* (2004). New families of TWs have also been reported in Pringle & Kerswell

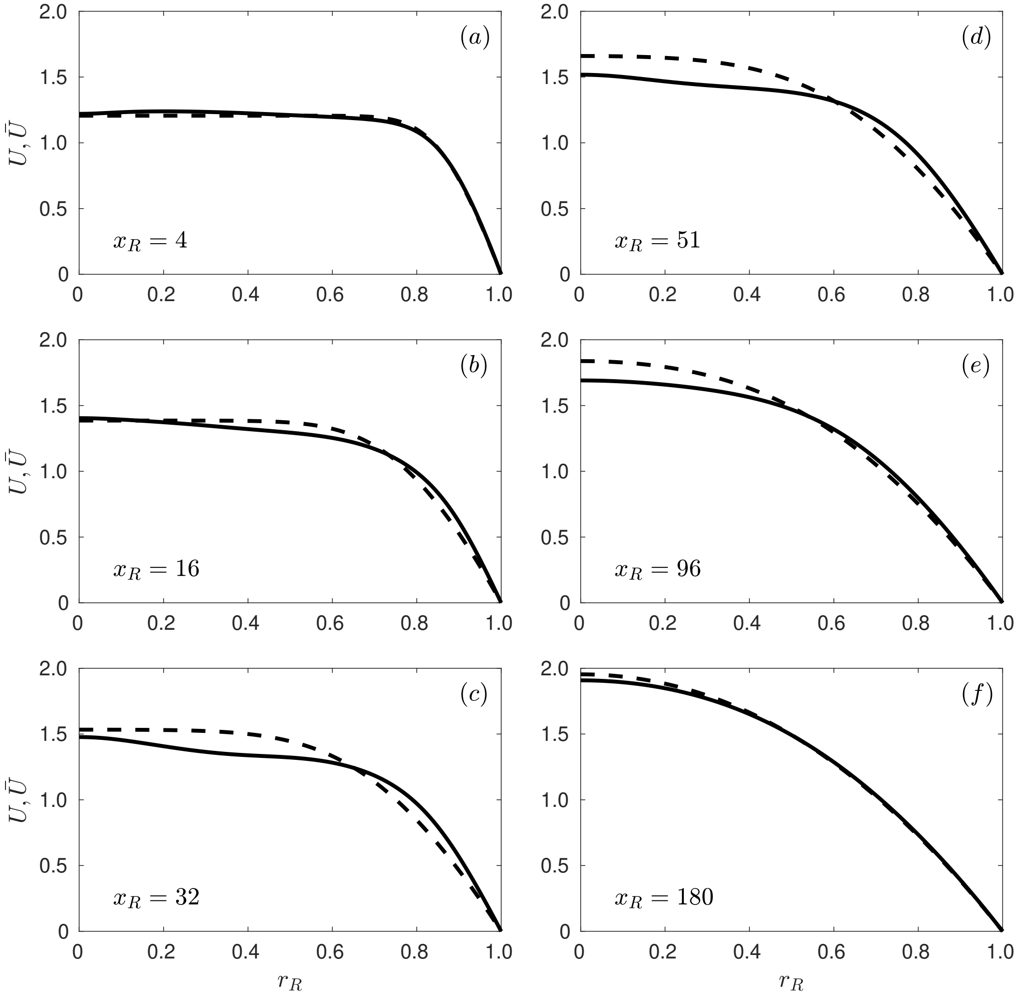

Figure 8: Streamwise velocity profiles of the laminar base flow U (dashed line) and the distorted mean flow $\bar{U} = U + r_t \hat{u}_{0,0}$ (solid line) at different streamwise locations.

(2007) and Pringle *et al.* (2009). These TWs are nonlinear solutions of the Navier–Stokes equations and they capture distinct features of coherent structures observed in turbulent pipe flow (Graham & Floryan 2021). Willis & Kerswell (2008) suggested that these TWs populate an intermediate region between the laminar and turbulent states in phase space. However, the physical origin of these TWs has not been discussed and remains unclear.

As shown in figure 11, excellent visual agreement occurs between the $\mathcal{R}_3$-TW (where $\mathcal{R}_h$ represents the h-fold rotational symmetry) found by Wedin & Kerswell (2004) and the $\mathcal{R}_3$-EPENS at the same Reynolds number, $Re_R = 900$. (The Reynolds number based on the pipe diameter used in Wedin & Kerswell (2004), Willis *et al.* (2017) and Kerswell & Tutty (2007) has been converted to Re_R herein.) The EPENS are shown at $x_R = 18$ and $\bar{t} = 0$, where $u_{urm,max}$ attains the largest amplitude. Remarkable agreement is observed for the streamwise vortices and the high/low-speed streaks, although the TWs are found in fully developed pipe flow while the EPENS exist in the pipe entrance region. Both the $\mathcal{R}_3$-TW and $\mathcal{R}_3$-EPENS have three equispaced low-speed streaks (dark) located towards the centre and three equispaced high-speed streaks (light) positioned near the wall. For both sets of

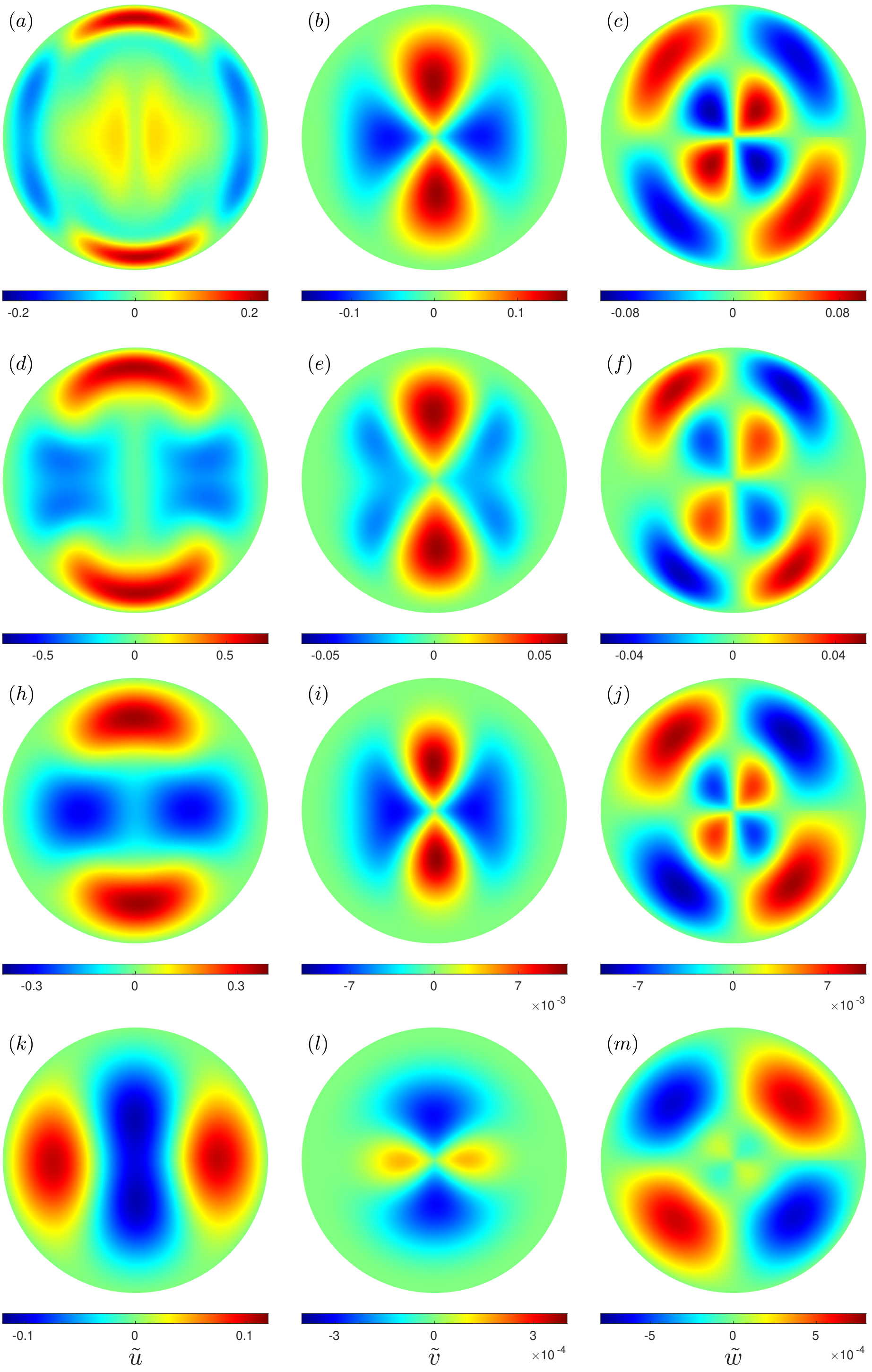

Figure 9: Contours of the velocity components $\tilde{u}$, $\tilde{v}$ and $\tilde{w}$ (from left to right) at the time instant $\bar{t} = 0$ and four different locations $x_R = 4, 26, 60, 150$ (from top to bottom), where the red/blue coloured shading indicates velocity faster/slower than the laminar base-flow velocity U. The same shading is used in figure 10.

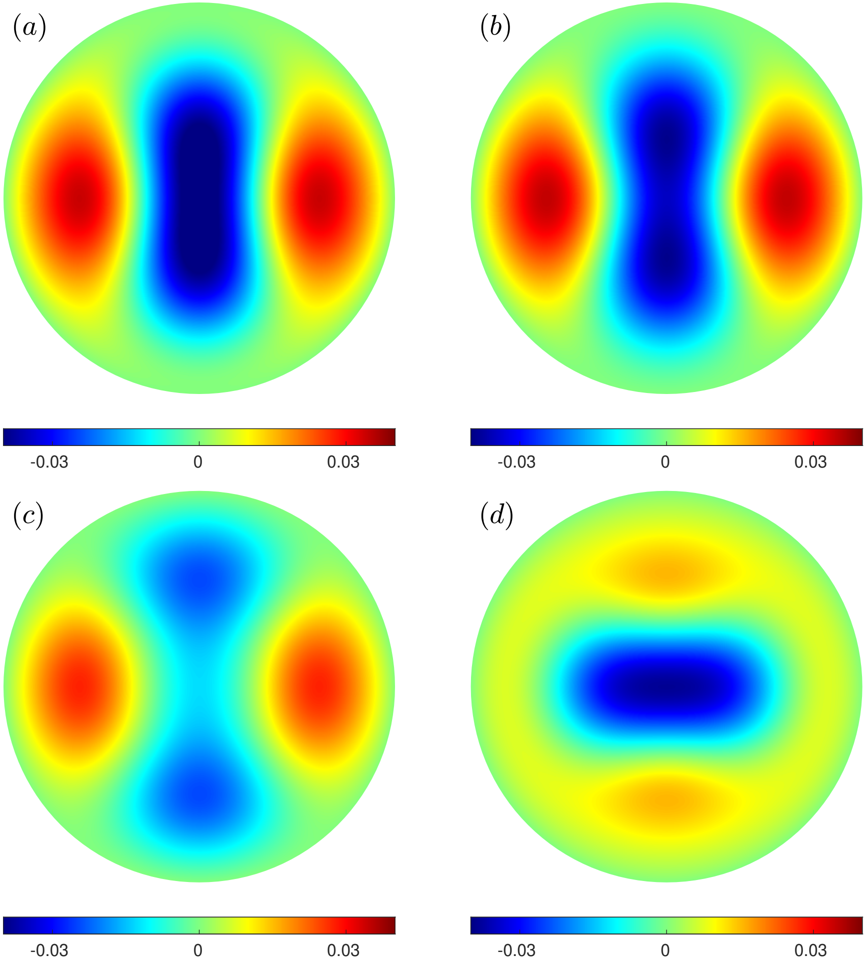

Figure 10: Contours of the streamwise velocity $\tilde{u}$ at the streamwise location $x_R = 200$ and four different time phases (*a*) $\bar{t} = 0$, (*b*) $\bar{t} = \pi/4$, (*c*) $\bar{t} = \pi/2$, and (*d*) $\bar{t} = 3\pi/4$.

nonlinear structures, streamwise vortices are located between adjacent low-speed and high-speed streaks, moving fluid towards the pipe axis in correspondence with low-speed streaks and wallward where high-speed streaks exist.

The TWs originate mathematically from saddle–node bifurcations and are calculated using a homotopy approach. However, this numerical method does not explain the physical origin of TWs. The method to compute the EPENS instead describes the physical origin of EPENS, i.e. the EPENS arise from the algebraic growth, nonlinear interactions and streamwise stretching of realistic vortical disturbances convected by the uniform flow approaching and entering the pipe inlet. We note that other receptivity mechanisms, such as wall vibration or roughness, could also create them. Wedin & Kerswell (2004) found that multiple solution branches coexist at higher Reynolds numbers (refer to figure 10 of Wedin & Kerswell (2004)). Besides the $\mathcal{R}_h$ solution shown in figure 11(*a*), which consists of h high-speed streaks near the wall, Wedin & Kerswell (2004) also discovered solutions with $2h$ near-wall high-speed streaks in other branches. Only EPENS with h high-speed streaks are instead found in our computations.

With figure 11(*b*) as a reference, computations of EPENS for $m_0 = 3$ are carried out for different Re_R, $k_{x,R}$ and l. The results are displayed in figure 12 at the locations where the

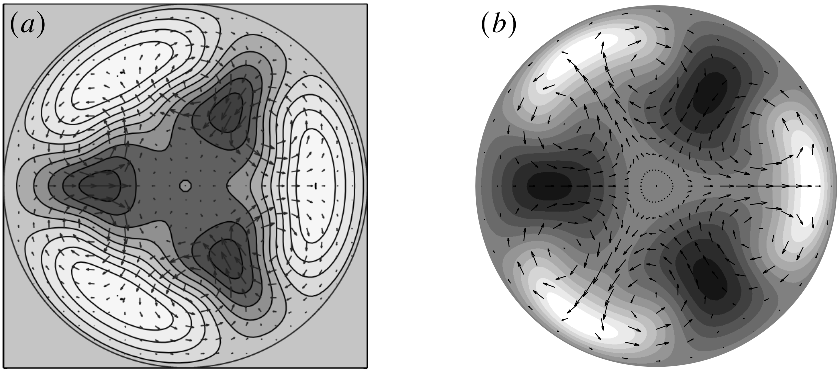

Figure 11: Comparison of velocity fields between the $\mathcal{R}_3$-TW and $\mathcal{R}_3$-EPENS for $Re_R = 900$. The cross-section vectors $\tilde{v}\boldsymbol{j} + \tilde{w}\boldsymbol{k}$ (where $\boldsymbol{j}$ and $\boldsymbol{k}$ are unit vectors in the radial and azimuthal directions) are indicated by arrows. The streamwise velocity $\tilde{u}$ is indicated by the shading, where light/dark colour indicates $\tilde{u}$ faster/slower than the laminar base-flow velocity U. The same shading is used in figures 12, 13 and 14. (*a*) The $\mathcal{R}_3$-TW found by Wedin & Kerswell (2004). (*b*) The $\mathcal{R}_3$-EPENS calculated at $x_R = 18$, where they are most amplified, and $\bar{t} = 0$ with $\epsilon = 0.05$, $k_{x,R} = 0.02$, $l = 3$ and $m_0 = 3$.

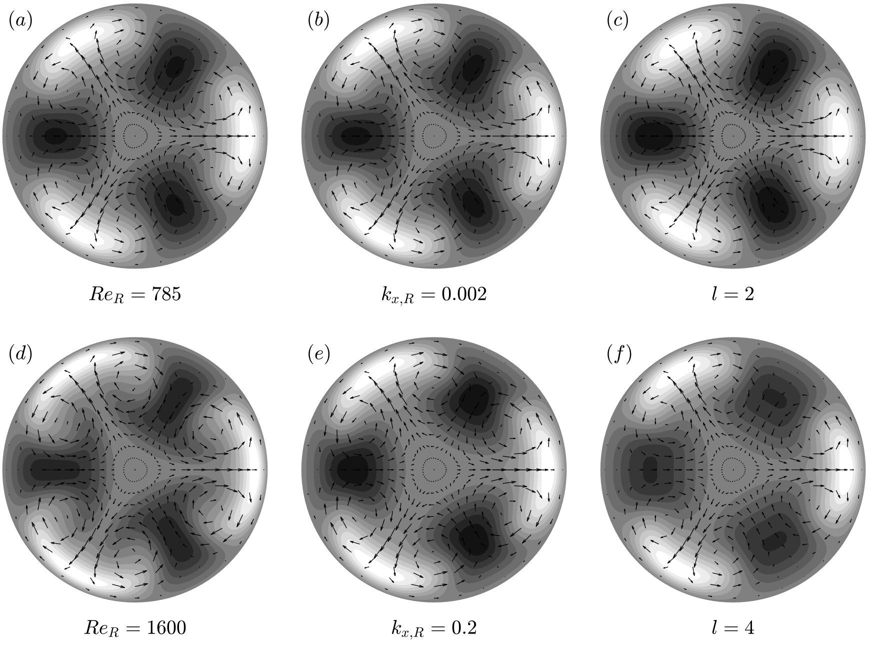

$Re_R = 785$ $k_{x,R} = 0.002$ $l = 2$

$Re_R = 1600$ $k_{x,R} = 0.2$ $l = 4$

Figure 12: Velocity fields of $\mathcal{R}_3$-EPENS at locations where they are most amplified and $\bar{t} = 0$ for different Re_R, $k_{x,R}$ and l. Unless otherwise stated, the parameters are $\epsilon = 0.05$, $Re_R = 900$, $k_{x,R} = 0.02$, $l = 3$ and $m_0 = 3$. (*a*) $Re_R = 785$, $x_R = 17$. (*b*) $k_{x,R} = 0.002$, $x_R = 18$. (*c*) $l = 2$, $x_R = 22$. (*d*) $Re_R = 1600$, $x_R = 19$. (*e*) $k_{x,R} = 0.2$, $x_R = 15$. (*f*) $l = 4$, $x_R = 20$.

EPENS are most amplified. Figure 11(*a*) corresponds to solution *a* in figure 10 of Wedin & Kerswell (2004), which was used for the branch continuation. This branch was traced down to $Re_R = 785$ and up to $Re_R = 1600$. Figures 12(*a*) and 12(*d*) show the EPENS calculated at these two Reynolds numbers. The similarities in the dominant streaks and vortices of

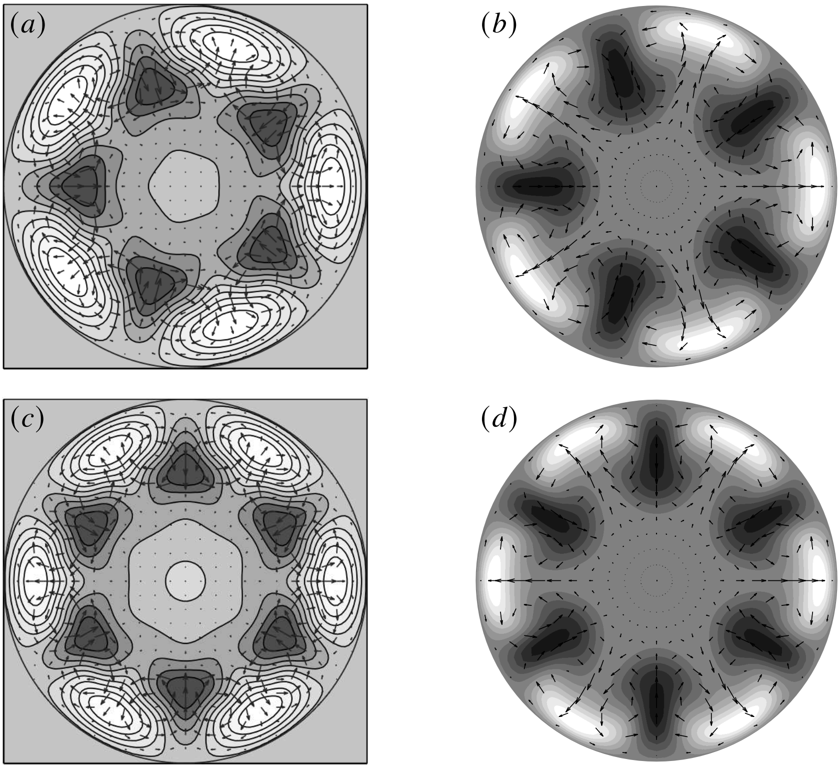

Figure 13: Comparison of velocity fields between TWs and EPENS for rotational symmetries $\mathcal{R}_5$ at $Re_R = 1242.75$ and $\mathcal{R}_6$ at $Re_R = 1434.5$. (a, c) The $\mathcal{R}_5$- and $\mathcal{R}_6$-TW found by Wedin & Kerswell (2004) at their saddle-node bifurcations. (b, d) The $\mathcal{R}_5$- and $\mathcal{R}_6$-EPENS calculated at $x_R = 12$ and 11, where they are most amplified, and $\bar{t} = 0$ for $\epsilon = 0.05$, $k_{x,R} = 0.02$, $l = 3$, and $m_0 = 5, 6$.

EPENS for different Re_R are observed. As Re_R increases, the low-speed streaks appear slightly narrower along the azimuthal direction, and the high-speed streaks become slightly more flattened towards the wall. The close resemblance among TWs pertaining to the same branch for different Re_R was also reported in Wedin & Kerswell (2004). Figures 12(b) and 12(e) show that varying the frequency by one hundred times has only a minimal impact on the EPENS. The robustness of the EPENS is further confirmed in figures 12(b) and 12(e) by varying the radial modulation of the inlet perturbation flow, given by the change of the parameter l. Increasing l, indicating an inlet perturbed flow with a smaller radial length scale, has only a mild influence on the EPENS. This result proves that the EPENS are likely to be a strong attractor of the dynamical system.

Except for the $\mathcal{R}_3$ symmetry, only TWs at their saddle-node bifurcations are presented for other rotational symmetry in Wedin & Kerswell (2004). Among these solutions, $\mathcal{R}_5$- and $\mathcal{R}_6$-TWs consist of h high-speed streaks near the wall, while $\mathcal{R}_1$-, $\mathcal{R}_2$- and $\mathcal{R}_4$-TWs have $2h$ high-speed streaks. Remarkable agreement between TWs and EPENS is also obtained for the $\mathcal{R}_5$ and $\mathcal{R}_6$ rotational symmetries, as reported in figure 13. The EPENS with h-fold rotational symmetry observed downstream is always excited by free-stream vortical disturbances with azimuthal wavenumber $m_0 = h$. The discovery of $\mathcal{R}_1$-TWs, which possess no discrete rotational symmetry, was reported in Pringle & Kerswell (2007). These TWs are more important than the rotationally symmetric ones because the upper/lower branches correspond to much higher/lower wall-shear stress values compared to rotationally symmetric

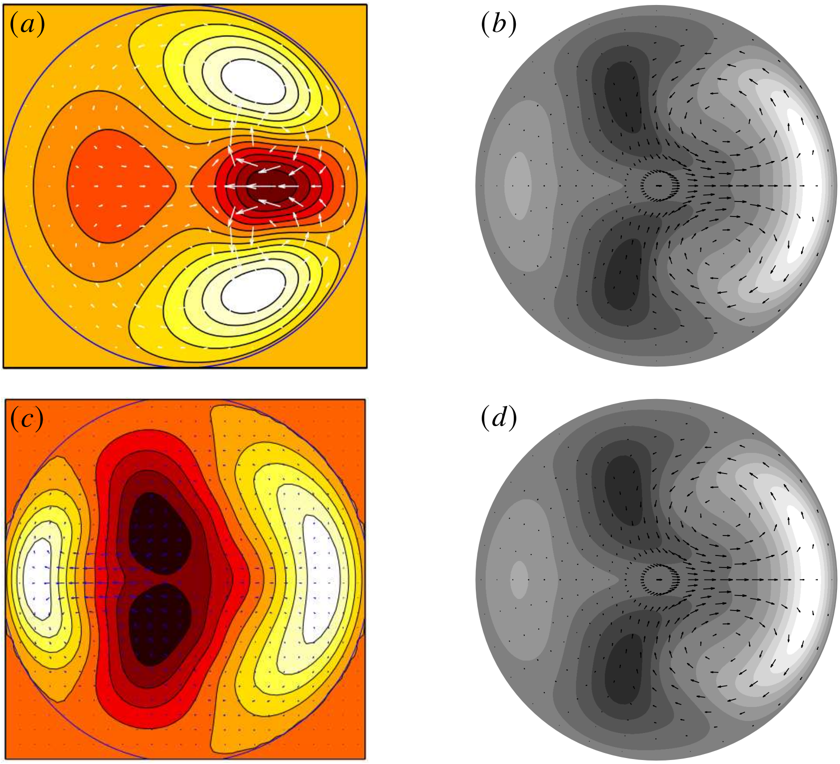

Figure 14: Comparison of velocity fields between the asymmetric TWs and $\mathcal{R}_1$-EPENS for $Re_R = 1450$ (a, b) and 1340 (c, d). (a, c) The asymmetric TWs found by Pringle & Kerswell (2007) and Willis *et al.* (2017), where the white/dark coloured shading indicates $\tilde{u}$ faster/slower than the laminar base-flow velocity U. (b, d) The $\mathcal{R}_1$-EPENS calculated at $x_R = 36$, where they are most amplified, and $\bar{t} = 0$ with $\epsilon = 0.05$, $k_{x,R} = 0.02$, $l = 3$, and $m_0 = 1$.

ones. Figure 14(a) shows the velocity field of an asymmetric TW of these new families. One low-speed streak is centred at half the distance between the wall and the centreline, and is surrounded by two high-speed streaks. As shown in figure 14(b), rotationally asymmetric EPENS are also found in our calculation when $m_0 = 1$. However, they consist of one wide near-wall high-speed streak flanked by two low-speed streaks, and one low-intensity high-speed streak on the opposite side of the wide high-speed streak. The cross-section velocity vector field reveals that counter-rotating streamwise vortices occur between the high-speed and the low-speed streaks. Using a feedback control strategy, a new asymmetric TW was identified by Willis *et al.* (2017) (figure 14(c)). Good agreement is noted between the streaks of their TW and our $\mathcal{R}_1$-EPENS at the same Reynolds number, whereas only very weak streamwise vortices are found between the wide high-speed streak and low-speed streaks in their case.

The comparison of streamwise velocity isosurfaces of the $\mathcal{R}_3$-TW calculated by Kerswell & Tutty (2007) and the $\mathcal{R}_3$-EPENS at $Re_R = 1200$ is also very good, as shown in figure 15, where the light and dark shadings denote the streamwise velocity for $\tilde{u} = 0.3U$ and $-0.3U$. The $\mathcal{R}_3$-TW is displayed versus its wavelength (the diameter of the pipe is used as a reference length), while the $\mathcal{R}_3$-EPENS is displayed for $13 < x_R < 17$. Along these distances, both the near-wall high-speed streaks and the low-speed streaks near the pipe core for both the TW and EPENS evolve slowly in the streamwise direction.

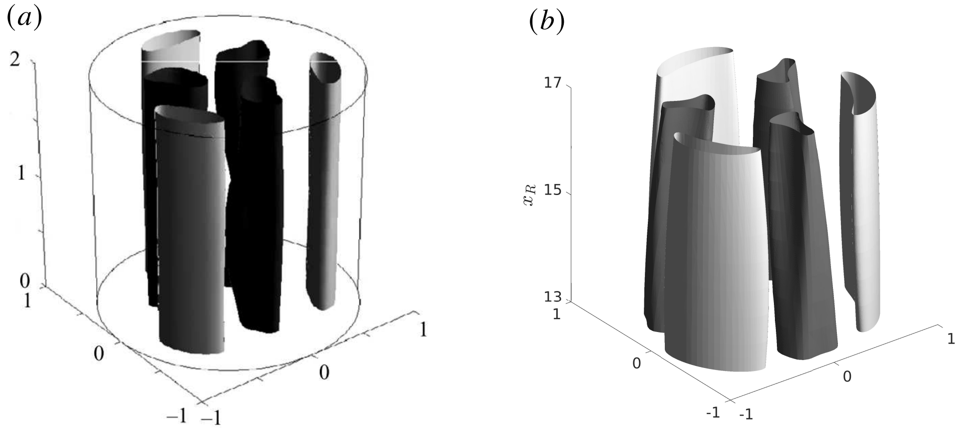

Figure 15: Comparison of streamwise velocity isosurfaces between the $\mathcal{R}_3$-TW and $\mathcal{R}_3$-EPENS for $Re_R = 1200$. The light and dark shading represents the streamwise velocity $\tilde{u}$ that equals $0.3U$ and $-0.3U$. (*a*) The $\mathcal{R}_3$-TW over the wavelength found by Kerswell & Tutty (2007). (*b*) The $\mathcal{R}_3$-EPENS calculated for $13 \ll x_R \ll 17$ and $\bar{t} = 0$ with $\epsilon = 0.05$, $k_{x,R} = 0.2$, $l = 3$ and $m_0 = 3$.

Considering the richness of the phase space, further comparison between TWs and EPENS for different parameters are warranted to fully understand their connection. One challenge in searching for an TW is the daunting numerical process required to find a good initial guess, whereas EPENS can be calculated much more rapidly using our approach. It is therefore suggested that EPENS could be used as initial guesses in the search for TWs.

3.4. *Comparison with experimental data*

Ricco & Alvarenga (2022) compared their linearised numerical results to the experimental measurements by Wygnanski & Champagne (1973). For both the mean and perturbation flow, excellent agreement was obtained at a low level of free-stream turbulence intensity, while a significant deviation between the linear results and the experimental data was reported for higher intensities. In figure 16, the experimental data at high turbulence intensity are compared with our nonlinear results. The turbulence intensity was measured by $(u_{rms}/\bar{U})_{cl}$ in Wygnanski & Champagne (1973), where the subscript cl refers to the value at the pipe axis. The values of $(u_{rms}/\bar{U})_{cl} = 5.8\%$ and 7.8% in Wygnanski & Champagne (1973) are found to be equivalent to $\epsilon = 0.082$ and 0.12 in our calculation for the case with $k_{x,R} = 0.118$, $l = 2$ and $m_0 = 2$. Figure 16(*a*) shows the good agreement in the mean-flow velocity profiles except in the near-wall region where the numerical calculations underpredict the experimental data. Good agreement also occurs in the comparison of the perturbation-flow velocity profiles, as shown in figure 16(*b*). In Ricco & Alvarenga (2022), the velocity profile was instead predicted by the linearised boundary-region equations to be zero at the pipe axis. The finite perturbations near the pipe axis are well predicted when the nonlinear interactions (i.e. $r_t \hat{u}_{0,0}$) are taken into account. Both studies show the same trend: as the turbulent intensity increases, a larger peak is reached, and the peak position moves towards the wall. The peak of the profiles measured by Wygnanski & Champagne (1973) is obtained at a lower value and located closer to the wall compared to our calculations. The disagreements are likely to come from the different inflows at the pipe inlet. In experiments, the disturbances were generated by an orifice plate or a circular disk placed at the inlet, and no precise information about the resulting initial flow was given. The analytical expression (2.1) is instead used to model the vortical disturbances in our calculations. As the flow is described by an initial-boundary

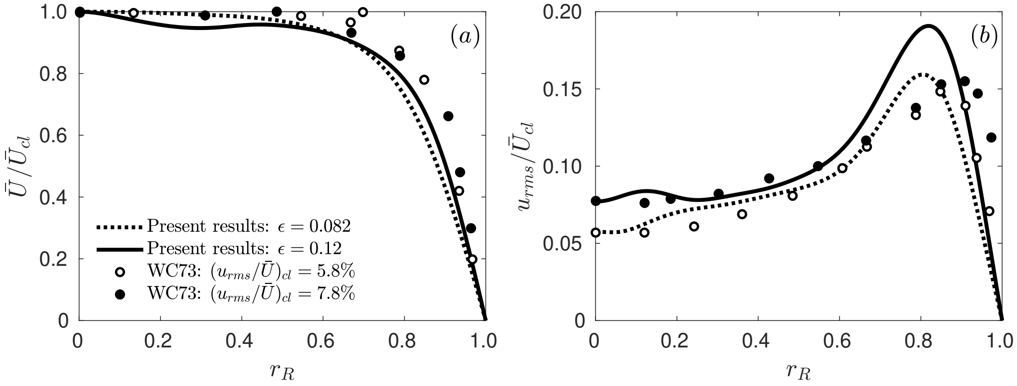

Figure 16: Comparison of (a) the mean flow and (b) the perturbation flow between the experimental measurements (circles) and present numerical results (lines) for $Re_R = 1200$ at $x_R = 30$. Open and solid circles: experimental data measured by Wygnanski & Champagne (1973) (refer to as WC73 in the figure) with $(u_{rms}/\bar{U})_{cl} = 5.8\%$ and 7.8%. Dotted and solid lines: present results with $\epsilon = 0.082, 0.12$, $k_{x,R} = 0.118$, $l = 2$ and $m_0 = 2$.

value problem in the pipe entrance, the inflow characteristics are crucial for an accurate prediction of the downstream development of the flow.

4. Summary and conclusions

As a step towards understanding the laminar–turbulent transition in pipe flow, we have investigated the nonlinear evolution of free-stream vortical disturbances entrained in the entrance region of a circular pipe by using a high Reynolds number asymptotic approach. The oncoming disturbances are modelled by a pair of vortical modes with the same frequency but opposite azimuthal wavenumber. A long-wavelength hypothesis is utilised. This hypothesis is inspired by the experimental finding that streamwise-elongated streaks induced by free-stream disturbances in boundary layers amplify significantly (Matsubara & Alfredsson 2001). The disturbance amplitude is assumed to be intense enough for nonlinear interactions to occur. The present study can therefore be viewed as an extension of Ricco & Alvarenga (2022) to the nonlinear case.

The resultant nonlinear system is solved numerically by a marching procedure in the streamwise direction. A parametric study reveals the stabilising effect of nonlinearity on the intense algebraic disturbance growth near the pipe inlet. The linear theory thus overpredicts the nonlinear disturbance intensity. The effect of the Reynolds number, the streamwise and azimuthal wavelengths, and the radial length scale of the inlet disturbance on the nonlinear evolution of the disturbances is investigated. The mean-flow distortion $\hat{u}_{0,0}$ grows significantly shortly downstream of the pipe inlet, being negative in the pipe core and positive near the wall, indicating an increase of wall-shear stress.

We report the formation, amplification and attenuation of rotationally symmetric elongated pipe-entrance nonlinear structures (EPENS). The distinct features of $\mathcal{R}_h$-EPENS ($h > 1$) are equispaced h high-speed streaks around the pipe wall and h low-speed streaks in the pipe core. A remarkable resemblance between these structures and nonlinear travelling waves (TWs) occurring in fully developed pipe flow is noted for $m_0 = 3, 5, 6$. Rotationally asymmetric EPENS are discovered for $m_0 = 1$. They also agree well with asymmetric TWs for $m_0 = 1$. These similarities may shed light on the physical origin of nonlinear TWs. The robustness of the EPENS in response to changes of different inlet flow conditions is demonstrated, indicating that the EPENS are likely to be a strong attractor of the dynamical system. We also suggest the potential use of EPENS as an initial guess in the numerical search for the nonlinear TWs. More investigations are necessary to clarify the connection between the EPENS and the TWs.

With the inclusion of nonlinear effects, good agreement between our calculations and the experimental measurements of Wygnanski & Champagne (1973) is obtained for both the mean flow and the perturbation flow. Further improvement may be gained by using a continuous spectrum of free-stream disturbances as oncoming disturbances. Performing a secondary instability analysis of the EPENS is also of interest. The EPENS attenuate downstream in our calculation, but they may persist when the growth of small-amplitude secondary disturbances is taken into account.

It is our hope that the theoretical work presented herein will motivate more direct numerical simulations and experimental investigations in the entrance region of pipe flow.

Acknowledgements. The authors would like to thank the Faculty of Engineering of the University of Sheffield for funding this research. The authors are also indebted to Dr Elena Marensi for her insightful comments.

Funding. This work was funded by Faculty of Engineering University Research Scholarship from University of Sheffield.

Declaration of interests. The authors report no conflict of interest.

Appendix A. Conservation of the mass flow rate

At each instant in time and at each streamwise location, the mass flow rate is conserved. Since the flow is incompressible, this condition translates to the conservation of the bulk velocity, i.e. the streamwise velocity averaged on the cross-section of the pipe is equal to the oncoming velocity U^*_∞:

$$\frac{1}{\pi R^2}\int_0^{2\pi}\int_0^R (U + r_t\bar{u})\, r\mathrm{d}r\mathrm{d}\theta = 1. \tag{A 1}$$

Substituting (2.7) into (A 1), equation (2.11) is obtained for the laminar base flow and

$$\sum_{m,n=-\infty}^{\infty}\int_0^{2\pi}\int_0^R \hat{u}_{m,n}e^{im\theta+in\bar{t}}\, r\mathrm{d}r\mathrm{d}\theta = 0. \tag{A 2}$$

By using the orthogonality property of the Fourier series, equation (2.20) is obtained, which is the condition needed to solve the system because the pressure $\Gamma_{0,n}$ is an additional unknown.

Appendix B. Coefficients of equation (2.27)

The expressions of $\{\widehat{V}, \widehat{V}_r, \widehat{V}_x, \cdots, \widehat{U}_{xrr}\}$ in equation (2.27) are

$$\widehat{V} = \left(1 - \frac{1}{m^2}\right)\left(in + \frac{\partial V}{\partial r} + \frac{m^2-1}{\mathcal{F}r^2}\right) + \frac{2r}{m^2}\frac{\partial^2 U}{\partial \bar{x}\partial r} + \frac{r^2}{m^2}\frac{\partial^3 U}{\partial \bar{x}\partial r^2},$$

$$\widehat{V}_r = \left[\left(1 - \frac{4}{m^2}\right)V - \frac{3r}{m^2}\left(in + \frac{\partial V}{\partial r}\right) - \left(2 + \frac{1}{m^2}\right)\frac{1}{\mathcal{F}r}\right] + \frac{r^2}{m^2}\frac{\partial^2 U}{\partial \bar{x}\partial r},$$

$$\widehat{V}_x = \left(1 - \frac{1}{m^2}\right)U + \frac{r}{m^2}\left(\frac{\partial U}{\partial r} + r\frac{\partial^2 U}{\partial r^2}\right),$$

$$
\begin{aligned}
\widehat{V}_{rr} &= -\left[\frac{r}{m^2}\left(inr + 5V + r\frac{\partial V}{\partial r}\right) + \left(2 - \frac{5}{m^2}\right)\frac{1}{\mathcal{F}}\right],\\
\widehat{V}_{xr} &= -\frac{3Ur}{m^2},\\
\widehat{V}_{rrr} &= -\frac{r}{m^2}\left(rV - \frac{6}{\mathcal{F}}\right),\\
\widehat{V}_{xrr} &= -\frac{r^2U}{m^2},\\
\widehat{V}_{rrrr} &= \frac{r^2}{m^2\mathcal{F}},\\
\widehat{U} &= \frac{\partial V}{\partial \bar{x}} + \frac{2r}{m^2}\frac{\partial^2 U}{\partial \bar{x}^2} + \frac{r^2}{m^2}\frac{\partial^3 U}{\partial \bar{x}^2 \partial r},\\
\widehat{U}_r &= \frac{r}{m^2}\frac{\partial V}{\partial \bar{x}},\\
\widehat{U}_x &= -\frac{2}{\mathcal{F}r} + \frac{6r}{m^2}\frac{\partial U}{\partial \bar{x}} + \frac{2r^2}{m^2}\frac{\partial^2 U}{\partial \bar{x}\partial r},\\
\widehat{U}_{rr} &= \frac{r^2}{m^2}\frac{\partial V}{\partial \bar{x}},\\
\widehat{U}_{xr} &= \frac{2}{m^2}\left(\frac{1}{\mathcal{F}} - 2Vr - r^2\frac{\partial V}{\partial r}\right),\\
\widehat{U}_{xrr} &= \frac{2r}{m^2\mathcal{F}}.
\end{aligned}
$$

Appendix C. Modified block tridiagonal matrix algorithm

A modified block tridiagonal matrix algorithm is devised for solving the discretised version of system (2.30)-(2.32) together with the discretised (2.20) for $m = 0$,

$$\boldsymbol{A}\boldsymbol{\delta} = \boldsymbol{b}. \tag{C 1}$$

In expanded form, the system (C 1) is

$$
\left[\begin{array}{cccccccc}
A_1 & C_1 & & & & & & E_1\\
B_2 & A_2 & C_2 & & & & & E_2\\
 & \cdots & \cdots & \cdots & & & & \cdots\\
 & & B_j & A_j & C_j & & & E_j\\
 & & & \cdots & \cdots & \cdots & & \cdots\\
 & & & & B_{J-3} & A_{J-3} & C_{J-3} & E_{J-3}\\
 & & & & & B_{J-2} & A_{J-2} & E_{J-2}\\
D_1 & D_2 & D_3 & & \cdots & & D_{J-2} & 0
\end{array}\right]
\left[\begin{array}{c}
\delta_1\\ \delta_2\\ \cdots\\ \delta_j\\ \cdots\\ \delta_{J-3}\\ \delta_{J-2}\\ \Pi
\end{array}\right]
=
\left[\begin{array}{c}
b_1\\ b_2\\ \cdots\\ b_j\\ \cdots\\ b_{J-3}\\ b_{J-2}\\ 0
\end{array}\right] \tag{C 2}
$$

where A_j, B_j and C_j are 3×3 matrices, E_j, δ_j and b_j are 3×1 matrices, D_j is a 1×3 matrix, and Π is a scalar. In equation (C 2), row j for $2 \leqslant j \leqslant J-3$ represents the discretised equations (2.30)–(2.32) at the interior nodes, while rows 1 and $J-2$ refer to the equations at the boundaries. The last row is the discretised integral (2.20).

First, we add any two decoupled equations to the system in order to add two rows at the bottom of matrix $\boldsymbol{A}$ and two columns on the right of matrix $\boldsymbol{A}$. This step makes D_j and E_j 3×3 matrices, and creates two 3×1 matrices, δ_{J-1} and b_{J-1}, at the bottom of $\boldsymbol{\delta}$ and $\boldsymbol{b}$, which is necessary in order to render the system suitable for the block elimination. The matrices

D_j and E_j are renamed $\mathcal{D}_j$ and $\mathcal{E}_j$. The system (C 2) becomes

$$\begin{bmatrix} A_1 & C_1 & & & & & & \mathcal{E}_1 \\ B_2 & A_2 & C_2 & & & & & \mathcal{E}_2 \\ & \cdots & \cdots & \cdots & & & & \cdots \\ & & B_j & A_j & C_j & & & \mathcal{E}_j \\ & & & \cdots & \cdots & \cdots & & \cdots \\ & & & & B_{J-3} & A_{J-3} & C_{J-3} & \mathcal{E}_{J-3} \\ & & & & & B_{J-2} & A_{J-2} & \mathcal{E}_{J-2} \\ \mathcal{D}_1 & \mathcal{D}_2 & \mathcal{D}_3 & & \cdots & & \mathcal{D}_{J-2} & \mathcal{E}_{J-1} \end{bmatrix} \begin{bmatrix} \delta_1 \\ \delta_2 \\ \cdots \\ \delta_j \\ \cdots \\ \delta_{J-3} \\ \delta_{J-2} \\ \delta_{J-1} \end{bmatrix} = \begin{bmatrix} b_1 \\ b_2 \\ \cdots \\ b_j \\ \cdots \\ b_{J-3} \\ b_{J-2} \\ b_{J-1} \end{bmatrix} \tag{C 3}$$

The standard block tridiagonal matrix algorithm described in Cebeci (2002) is modified to solve (C 3), which also consists of the forward sweep and backward substitution. However, in each forward sweep, one more step needs to be performed to eliminate $\mathcal{D}_j$, which leads to

$$\begin{bmatrix} I & C'_1 & & & & & & \mathcal{E}'_1 \\ & I & C'_2 & & & & & \mathcal{E}'_2 \\ & & \cdots & \cdots & & & & \cdots \\ & & & I & C'_j & & & \mathcal{E}'_j \\ & & & & \cdots & \cdots & & \cdots \\ & & & & & I & C'_{J-3} & \mathcal{E}'_{J-3} \\ & & & & & & I & \mathcal{E}'_{J-2} \\ & & & & & & & \mathcal{E}'_{J-1} \end{bmatrix} \begin{bmatrix} \delta_1 \\ \delta_2 \\ \cdots \\ \delta_j \\ \cdots \\ \delta_{J-3} \\ \delta_{J-2} \\ \delta_{J-1} \end{bmatrix} = \begin{bmatrix} b'_1 \\ b'_2 \\ \cdots \\ b'_j \\ \cdots \\ b'_{J-3} \\ b'_{J-2} \\ b'_{J-1} \end{bmatrix} \tag{C 4}$$

where the prime denotes the new coefficients. The solution is then obtained by backward substitution:

$$\begin{cases} \delta_{J-1} = \mathcal{E}'^{-1}_{J-1} b'_{J-1}, \\ \delta_{J-2} = b'_{J-2} - \mathcal{E}'_{J-2}\delta_{J-1} \\ \delta_i = b'_i - C'_i\delta_{i+1} - \mathcal{E}'_i\delta_{J-1}, \quad i = J-3, J-4, \cdots, 1. \end{cases} \tag{C 5}$$

REFERENCES

Avila, M., Barkley, D. & Hof, B. 2023 Transition to turbulence in pipe flow. *Annu. Rev. Fluid Mech.* **55**, 575–602.

Batchelor, G.K. & Gill, A.E. 1962 Analysis of the stability of axisymmetric jets. *J. Fluid Mech.* **14**, 529–551.

Bergström, L. 1992 Initial algebraic growth of small angular dependent disturbances in pipe Poiseuille flow. *Stud. Appl. Maths.* **87** (1), 61–79.

Bergström, L. 1993 Optimal growth of small disturbances in pipe Poiseuille flow. *Phys. Fluids A* **5** (11), 2710–2720.

Borodulin, V. I., Ivanov, A. V., Kachanov, Y. S. & Roschektayev, A. P. 2021 Distributed vortex receptivity of a swept-wing boundary layer. Part 1. Efficient excitation of cf modes. *J. Fluid Mech.* **908**, A14.

Böberg, L. & Brösa, U. 1988 Onset of turbulence in a pipe. *Z. Naturforsch. A* **43** (8-9), 697–726.

Cebeci, T. 2002 *Convective heat transfer*. Springer.

Christiansen, E.B. & Lemmon, H.E. 1965 Entrance region flow. *AIChE J.* **11** (6), 995–999.

Corcos, G.M. & Sellars, J.R. 1959 On the stability of fully developed flow in a pipe. *J. Fluid Mech.* **5** (1), 97–112.

Crowder, H.J. & Dalton, C. 1971 On the stability of Poiseuille flow in a pipe. *J. Comp. Phys.* **7** (1), 12–31.

Davey, A. 1978 On Itoh's finite amplitude stability theory for pipe flow. *J. Fluid Mech.* **86** (4), 695–703.

Davey, A. & Drazin, P.G. 1969 The stability of Poiseuille flow in a pipe. *J. Fluid Mech.* **36** (2), 209–218.

Davey, A. & Nguyen, H.P.F. 1971 Finite-amplitude stability of pipe flow. *J. Fluid Mech.* **45** (4), 701–720.

DIETZ, A. J. 1999 Local boundary-layer receptivity to a convected free-stream disturbance. *J. Fluid Mech.* **378**, 291–317.

ECKHARDT, B., SCHNEIDER, T.M., HOF, B. & WESTERWEEL, J. 2007 Turbulence transition in pipe flow. *Annu. Rev. Fluid Mech.* **39** (1), 447–468.

FAISST, H. & ECKHARDT, B. 2003 Traveling waves in pipe flow. *Phys. Rev. Lett.* **91** (22), 224502.

GARG, V.K. 1981 Stability of developing flow in a pipe: non-axisymmetric disturbances. *J. Fluid Mech.* **110**, 209–216.

GARG, V.K. 1983 Stability of nonparallel developing flow in a pipe to nonaxisymmetric disturbances. *J. Appl. Mech.* **50** (1), 210.

GARG, V.K. & GUPTA, S.C. 1981 Stability of developing flow in a pipe-nonparallel effects. *J. Appl. Mech.* **48** (2), 243.

GARG, V.K. & ROULEAU, W.T. 1972 Linear spatial stability of pipe Poiseuille flow. *J. Fluid Mech.* **54** (1), 113–127.

GILL, A.E. 1965 On the behaviour of small disturbances to Poiseuille flow in a circular pipe. *J. Fluid Mech.* **21** (1), 145–172.

GRAHAM, M. D. & FLORYAN, D. 2021 Exact coherent states and the nonlinear dynamics of wall-bounded turbulent flows. *Annu. Rev. Fluid Mech.* **53** (Volume 53, 2021), 227–253.

GUPTA, S.C. & GARG, V.K. 1981 Effect of velocity distribution on the stability of developing flow in a pipe. *Phys. Fluids* **24** (4), 576–578.

HAGEN, G. 1839 Ueber die bewegung des wassers in engen cylindrischen röhren. *Annalen der Physik* **122** (3), 423–442.

HOF, B., VAN DOORNE, C.W.H., WESTERWEEL, J. & NIEUWSTADT, F.T.M. 2005 Turbulence regeneration in pipe flow at moderate Reynolds numbers. *Phys. Rev. Lett.* **95** (21), 214502.

HOF, B., VAN DOORNE, C.W.H., WESTERWEEL, J., NIEUWSTADT, F.T.M., FAISST, H., ECKHARDT, B., WEDIN, H., KERSWELL, R.R. & WALEFFE, F. 2004 Experimental observation of nonlinear traveling waves in turbulent pipe flow. *Science* **305** (5690), 1594–1598.

HORNBECK, R.W. 1964 Laminar flow in the entrance region of a pipe. *Appl. Sci. Res.* **13**, 224–232.

HUANG, L.M. & CHEN, T.S. 1974*a* Stability of the developing laminar pipe flow. *Phys. Fluids* **17** (1), 245–247.

HUANG, L.M. & CHEN, T.S. 1974*b* Stability of developing pipe flow subjected to non-axisymmetric disturbances. *J. Fluid Mech.* **63** (1), 183–193.

ITOH, N. 1977 Nonlinear stability of parallel flows with subcritical Reynolds numbers. Part 2. Stability of pipe Poiseuille flow to finite axisymmetric disturbances. *J. Fluid Mech.* **82** (3), 469–479.

KERSWELL, R.R. 2005 Recent progress in understanding the transition to turbulence in a pipe. *Nonlinearity* **18** (6), R17.

KERSWELL, R.R. 2018 Nonlinear nonmodal stability theory. *Annu. Rev. Fluid Mech.* **50** (1), 319–345.

KERSWELL, R.R., PRINGLE, C.C.T. & WILLIS, A.P. 2014 An optimization approach for analysing nonlinear stability with transition to turbulence in fluids as an exemplar. *Rep. Prog. Phys.* **77** (8), 085901.

KERSWELL, R.R. & TUTTY, O.R. 2007 Recurrence of travelling waves in transitional pipe flow. *J. Fluid Mech.* **584**, 69–102.

KHORRAMI, M.R., MALIK, M.R. & ASH, R.L. 1989 Application of spectral collocation techniques to the stability of swirling flows. *J. Comp. Phys.* **81** (1), 206–229.

LANGHAAR, H.L. 1942 Steady flow in the transition length of a straight tube. *J. Appl. Mech.* **9** (2), A55–A58.

LEIB, S.J., WUNDROW, D.W. & GOLDSTEIN, M.E. 1999 Effect of free-stream turbulence and other vortical disturbances on a laminar boundary layer. *J. Fluid Mech.* **380**, 169–203.

LEWIS, H.R. & BELLAN, P.M. 1990 Physical constraints on the coefficients of fourier expansions in cylindrical coordinates. *J. Math. Phys.* **31** (11), 2592–2596.

MARENSI, E. & RICCO, P. 2017 Growth and wall-transpiration control of nonlinear unsteady Görtler vortices forced by free-stream vortical disturbances. *Phys. Fluids* **29** (11), 114106.

MARENSI, E., RICCO, P. & WU, X. 2017 Nonlinear unsteady streaks engendered by the interaction of free-stream vorticity with a compressible boundary layer. *J. Fluid Mech.* **817**, 80–121.

MATSUBARA, M. & ALFREDSSON, P.H. 2001 Disturbance growth in boundary layers subjected to free-stream turbulence. *J. Fluid Mech.* **430**, 149–168.

MESEGUER, A. & TREFETHEN, L.N. 2003 Linearized pipe flow to Reynolds number 107. *J. Comp. Phys.* **186** (1), 178–197.

O'Sullivan, P.L. & Breuer, K.S. 1994 Transient growth in circular pipe flow. I. Linear disturbances. *Phys. Fluids* **6** (11), 3643–3651.

Patera, A.T. & Orszag, S.A. 1981 Finite-amplitude stability of axisymmetric pipe flow. *J. Fluid Mech.* **112**, 467–474.

Pekeris, C.L. 1948 Stability of the laminar flow through a straight pipe of circular cross-section to infinitesimal disturbances which are symmetrical about the axis of the pipe. *Proc. Natl Acad. Sci.* **34** (6), 285–295.

Pfenniger, W 1961 Transition in the inlet length of tubes at high reynolds numbers. *Boundary layer and flow control* pp. 970–980.

Poiseuille, J.L. 1844 *Recherches expérimentales sur le mouvement des liquides dans les tubes de très-petits diamètres*. Imprimerie Royale.

Pope, S.B. 2000 *Turbulent flows*. Cambridge University Press.

Pringle, C.C.T., Duguet, Y. & Kerswell, R.R. 2009 Highly symmetric travelling waves in pipe flow. *Phil. Trans. R. Soc. A* **367** (1888), 457–472.

Pringle, C.C.T. & Kerswell, R.R. 2007 Asymmetric, helical, and mirror-symmetric traveling waves in pipe flow. *Phys. Rev. Lett.* **99** (7), 074502.

Pringle, C.C.T. & Kerswell, R.R. 2010 Using nonlinear transient growth to construct the minimal seed for shear flow turbulence. *Phys. Rev. Lett.* **105**, 154502.

Pringle, C.C.T., Willis, A.P. & Kerswell, R.R. 2012 Minimal seeds for shear flow turbulence: using nonlinear transient growth to touch the edge of chaos. *J. Fluid Mech.* **702**, 415–443.

Rayleigh, L. 1892 On the question of the stability of the flow of fluids. *Philos. Mag.* **34** (206), 59–70.

Reshotko, E. & Tumin, A. 2001 Spatial theory of optimal disturbances in a circular pipe flow. *Phys. Fluids* **13** (4), 991–996.

Reynolds, O. 1883 XXIX. An experimental investigation of the circumstances which determine whether the motion of water shall be direct or sinuous, and of the law of resistance in parallel channels. *Phil. Trans. R. Soc.* (174), 935–982.

Ricco, P. & Alvarenga, C. 2021 Entrainment and growth of vortical disturbances in the channel-entrance region. *J. Fluid Mech.* **927**, A18.

Ricco, P. & Alvarenga, C. 2022 Growth of vortical disturbances entrained in the entrance region of a circular pipe. *J. Fluid Mech.* **932**, A16.

Ricco, P., Luo, J. & Wu, X. 2011 Evolution and instability of unsteady nonlinear streaks generated by free-stream vortical disturbances. *J. Fluid Mech.* **677**, 1–38.

Salwen, H. & Grosch, C.E. 1972 The stability of Poiseuille flow in a pipe of circular cross-section. *J. Fluid Mech.* **54** (1), 93–112.

Sarpkaya, T. 1975 A note on the stability of developing laminar pipe flow subjected to axisymmetric and non-axisymmetric disturbances. *J. Fluid Mech.* **68** (2), 345–351.

Schmid, P.J. 2007 Nonmodal stability theory. *Annu. Rev. Fluid Mech.* **39** (1), 129–162.

Schmid, P.J. & Henningson, D.S. 1994 Optimal energy density growth in Hagen–Poiseuille flow. *J. Fluid Mech.* **277**, 197–225.

Sexl, T. 1927 Zur stabilitätsfrage der Poiseuilleschen und Couetteschen strömung. *Ann. Phys.* **388** (14), 835–848.

Shen, F.C.T., Chen, T.S. & Huang, L.M. 1976 The effects of main-flow radial velocity on the stability of developing laminar pipe flow. *J. Appl. Mech.* **43** (2), 209.

da Silva, D.F. & Moss, E.A. 1994 The stability of pipe entrance flows subjected to axisymmetric disturbances. *J. Fluids Engng* **116** (1), 61–65.

Smith, F.T. & Bodonyi, R.J. 1982 Amplitude-dependent neutral modes in the Hagen-Poiseuille flow through a circular pipe. *Proc. R. Soc. Lond. A* **384** (1787), 463–489.

Sparrow, E.M., Lin, S.H. & Lundgren, T.S. 1964 Flow development in the hydrodynamic entrance region of tubes and ducts. *Phys. Fluids* **7** (3), 338–347.

Tatsumi, T. 1952 Stability of the laminar inlet-flow prior to the formation of Poiseuille regime, II. *J. Phys. Soc. Japan* **7** (5), 495–502.

Tuckerman, L.S. 1989 Divergence-free velocity fields in nonperiodic geometries. *J. Comp. Phys.* **80** (2), 403–441.

Tumin, A. 1996 Receptivity of pipe Poiseuille flow. *J. Fluid Mech.* **315**, 119–137.

Waleffe, F. 1997 On a self-sustaining process in shear flows. *Phys. Fluids* **9** (4), 883–900.

WEDIN, H. & KERSWELL, R.R. 2004 Exact coherent structures in pipe flow: travelling wave solutions. *J. Fluid Mech.* **508**, 333–371.

WILLIS, A. P., DUGUET, Y., OMEL'CHENKO, O. & WOLFRUM, M. 2017 Surfing the edge: using feedback control to find nonlinear solutions. *J. Fluid Mech.* **831**, 579–591.

WILLIS, A. P. & KERSWELL, R. R. 2008 Coherent structures in localized and global pipe turbulence. *Phys. Rev. Lett.* **100** (12), 124501.

WU, X., MOIN, P. & ADRIAN, R.J. 2020 Laminar to fully turbulent flow in a pipe: scalar patches, structural duality of turbulent spots and transitional overshoot. *J. Fluid Mech.* **896**, A9.

WU, X., MOIN, P., ADRIAN, R.J. & BALTZER, J.R. 2015 Osborne Reynolds pipe flow: Direct simulation from laminar through gradual transition to fully developed turbulence. *Proc. Natl Acad. Sci.* **112** (26), 7920–7924.

WYGNANSKI, I.J. & CHAMPAGNE, F.H. 1973 On transition in a pipe. Part 1. The origin of puffs and slugs and the flow in a turbulent slug. *J. Fluid Mech.* **59** (2), 281–335.

WYGNANSKI, I., SOKOLOV, M. & FRIEDMAN, D. 1975 On transition in a pipe. Part 2. The equilibrium puff. *J. Fluid Mech.* **69** (2), 283–304.

ZANOUN, E.-S., KITO, M. & EGBERS, C. 2009 A study on flow transition and development in circular and rectangular ducts. *J. Fluids Engng* **131** (6), 061204.